Draft version February 15, 2021
Typeset using LaTeX **twocolumn** style in AASTeX62

Radio Spectral Imaging of an M8.4 Eruptive Solar Flare: Possible Evidence of a Termination Shock

Yingjie Luo (骆英杰),[1] Bin Chen (陈彬),[1] Sijie Yu (余思捷),[1] Timothy S. Bastian,[2] and Samuel Krucker[3]

[1] *Center for Solar-Terrestrial Research, New Jersey Institute of Technology, 323 M L King Jr Blvd, Newark, NJ 07102-1982, USA*
[2] *National Radio Astronomy Observatory, 520 Edgemont Road Charlottesville, VA 22903-2475, USA*
[3] *University of Applied Sciences and Arts Northwestern Switzerland, 5210 Windisch, Switzerland*

Submitted to ApJ

ABSTRACT

Solar flare termination shocks have been suggested as one of the viable mechanisms for accelerating electrons and ions to high energies. Observational evidence of such shocks, however, remains rare. Using radio dynamic spectroscopic imaging of a long-duration C1.9 flare obtained by the Karl G. Jansky Very Large Array (VLA), Chen et al. (2015) suggested that a type of coherent radio bursts, referred to as "stochastic spike bursts", were radio signature of nonthermal electrons interacting with myriad density fluctuations at the front of a flare termination shock. Here we report another stochastic spike burst event recorded during the extended energy release phase of a long-duration M8.4-class eruptive flare on 2012 March 10. VLA radio spectroscopic imaging of the spikes in 1.0–1.6 GHz shows that, similar to the case of Chen et al. (2015), the burst centroids form an extended, $\sim 10''$-long structure in the corona. By combining extreme ultraviolet imaging observations of the flare from two vantage points with hard X-ray and ultraviolet observations of the flare ribbon brightenings, we reconstruct the flare arcade in three dimensions. The results show that the spike source is located at $\sim$60 Mm above the flare arcade where a diffuse supra-arcade fan and multitudes of plasma downflows are present. Although the flare arcade and ribbons seen during the impulsive phase do not allow us to clearly understand how the observed spike source location is connected to the flare geometry, cooling flare arcade observed two hours later suggest that the spikes are located in the above-the-loop-top region, where a termination shock presumably forms.

Keywords: Solar flares (1496), Shocks (2086), Solar coronal mass ejections (310), Solar radio emission (1522), Solar magnetic reconnection (1504), Non-thermal radiation sources (1119), Solar radio flares (1342)

1. INTRODUCTION

One of the core questions in the physics of the solar flares is how a large amount of magnetic energy is converted into other forms of energy, particularly the kinetic energy in flare-accelerated particles. Although magnetic reconnection has been widely accepted as the mechanism for releasing the magnetic energy, the physical mechanisms responsible for accelerating the charged particles to nonthermal energies remain uncertain (see, e.g., reviews by Miller et al. 1997; Zharkova et al. 2011). Among others, shocks are believed to be an important particle accelerator in many astrophysical and space plasma environments (e.g., Blandford & Ostriker 1978; Reynolds 2008; Burgess et al. 2012). Of particular interest in the context of solar flares is the solar flare termination shock, produced by supermagnetosonic reconnection outflows impinging upon the top of the newly formed flare arcades. Theoretical studies have shown that they could efficiently accelerate electrons and ions to high energies with a power-law spectral shape (Somov & Kosugi 1997; Tsuneta & Naito 1998; Mann et al. 2009; Warmuth et al. 2009; Guo & Giacalone 2012; Li et al. 2013; Nishizuka & Shibata 2013; Park et al. 2013; Kong et al. 2019, 2020).

Although solar flare termination shocks have been shown to exist in analytical calculations and numeri-

Corresponding author: Bin Chen
bin.chen@njit.edu

cal experiments (Forbes & Malherbe 1986; Forbes 1986, 1988; Seaton & Forbes 2009; Workman et al. 2011; Chen et al. 2015; Takasao et al. 2015; Takasao & Shibata 2016; Takahashi et al. 2017; Shen et al. 2018; Cai et al. 2019), and have been frequently depicted in schematics of the standard solar flare model (Masuda et al. 1994; Shibata et al. 1995; Magara et al. 1996; Forbes & Acton 1996; Lin & Forbes 2000), observational evidence for these shocks remains relatively rare. There have been only a handful of reports on possible signatures of flare termination shocks at radio, ultraviolet, and X-ray wavelengths (Masuda et al. 1994; Aurass et al. 2002; Aurass & Mann 2004; Mann et al. 2009; Warmuth et al. 2009; Chen et al. 2015, 2019; Guo et al. 2017; Polito et al. 2018; Cai et al. 2019; Tan et al. 2019; Fomichev & Chernov 2020). Here we refer interested readers to Chen et al. (2019) and references therein for more in-depth discussions regarding observational signatures of flare termination shocks, as well as possible reasons for the scarcity of these observations.

Using radio spectroscopic imaging observations obtained by the Karl G. Jansky Very Large Array (VLA; Perley et al. 2011) at 1–2 GHz, Chen et al. (2015) ("Chen15" hereafter) mapped the detailed morphology and dynamics of a termination shock in a GOES-class C1.9 eruptive flare, and located it at the ending point of fast plasma outflows above a looptop hard X-ray (HXR) source. The radio signature of the termination shock manifests itself in the time-frequency domain (i.e., radio "dynamic spectrum") as myriad decimetric stochastic spike bursts. Each spike burst is extremely short-lived (below the instrument time resolution of 50 ms; possibly down to several milliseconds) and has a narrow frequency bandwidth $\delta\nu/\nu$ (a few percent). Chen15 interpreted the emission for the spikes as linear mode conversion of Langmuir waves excited by accelerated nonthermal electrons as they interact with small-scale density fluctuations at the shock front. Therefore, the observed centroid location of each spike burst at a central frequency ν marks the site of the corresponding density fluctuation with a mean density of $n_e \approx ([\nu/\mathrm{Hz}]/8980)^2$ cm^{-3}. The narrow bandwidth is determined by the amplitude level of the density fluctuation $\delta\nu/\nu \approx \frac{1}{2}\delta n_e/n_e$ (Csillaghy & Benz 1993; Chen et al. 2015; Kontar et al. 2018). The short temporal scale is related to the small spatial scale of the density fluctuations and the impulsive nature of the plasma radiation process. Since each density fluctuation on the shock front may have a different mean density, the ensemble of the many spike source centroids that sample a range of different n_e values (for spike bursts observed in 1.0–1.8 GHz due to fundamental plasma radiation, the density range is 1.2–4.0×10^{10} cm^{-3}), in turn, outlines the detailed morphology of shock front at any given moment. Chen15 further showed that the disruption of the shock front coincides with the reduction of both of the nonthermal radio and HXR flux, implying the role of the termination shock in accelerating electrons to at least tens of keV.

We note that the decimetric stochastic spike bursts reported in Chen15 may or may not be the same phenomenon as the so-called "millisecond spike bursts" in the literature (e.g., Slottje 1978; Benz et al. 1982, 2002; Benz 1986; Gary et al. 1991; Guedel et al. 1991; Krucker et al. 1995; Altyntsev et al. 1995; Karlický et al. 1996; Paesold et al. 2001; Fleishman et al. 2003; Battaglia & Benz 2009; Cliver et al. 2011). In fact, they appear to share some similarities with the fine structures of type II radio bursts produced by propagating coronal shocks, when high-resolution dynamic spectral data are available (Chen et al. 2019). In all cases, we caution that one must be very careful when attributing an observed radio burst phenomenon with a certain appearance in the radio dynamic spectrum to given physical interpretation, particularly when imaging data is not available.

More recently, Chen et al. (2019) studied the split-band feature of the same event reported in Chen15 with detailed dynamic spectroscopic imaging observations. They found that the low-frequency branch of the radio spike bursts is located slightly above its high-frequency counterpart by ~0.8 Mm. Such a phenomenon is consistent with the scenario in which the split-band features are due to radio emission from the upstream and downstream sides of the shock front, respectively. This interpretation is in line with recent radio imaging results for split-band features observed in type II radio bursts (Zimovets et al. 2012; Chrysaphi et al. 2018; Zucca et al. 2018), yet their origin is still under debate. In this scenario, the frequency ratio between the high- and low-frequency split-band $\nu_{\mathrm{HF}}/\nu_{\mathrm{LF}}$ is determined by the density compression n_2/n_1 across the shock front. The shock Mach number M is found to be up to ~2.0, which is generally consistent with earlier predictions in analytical calculations and numerical experiments (Forbes 1986, 1988; Seaton & Forbes 2009; Takasao & Shibata 2016; Shen et al. 2018).

Here we report another decimetric stochastic spike burst event recorded by the VLA. The event was associated with a much stronger, GOES-class M8.4 eruptive flare from NOAA active region (AR) 11429 on 2012 March 10, seven days after the C1.9 limb event reported in the earlier studies (Chen et al. 2014, 2015, 2019). During this period, this AR rotated from the east limb location on 2012 March 3 to the western hemisphere (N17W24), providing a unique against-the-disk view of

the AR from multiple instruments. Using the same radio spectroscopic imaging technique, we derive the centroid location of the spike bursts at each time and frequency. The ensemble of the burst centroids again forms an elongated structure above the flare arcades in a diffuse supra-arcade fan structure where plasma downflows are present. The same supra-arcade fan and downflows, fortuitously, were observed by the Extreme Ultra-Violet Imager (EUVI; Wuelser et al. 2004) aboard one of the Solar Terrestrial Relations Observatory satellites (STEREO; Kaiser et al. 2008) from a limb-view perspective. Based on three-dimensional (3D) reconstruction of the flare arcades, we argue that the observed location and morphology of the stochastic spike bursts are consistent with the termination shock interpretation proposed in Chen15.

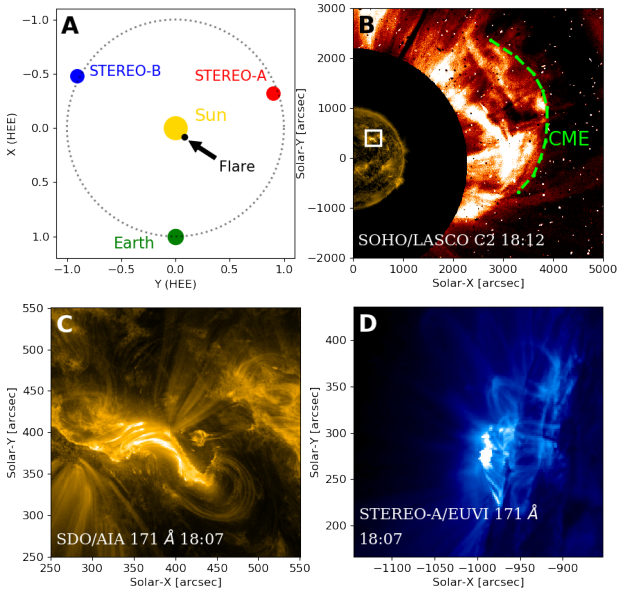

Figure 1. Overview of the SOL2012-03-10T17:14:40L280C090 M8.4 eruptive solar flare event. (A) Relative location of the Solar Dynamics Observatory (SDO; at a low Earth orbit) and the two STEREO satellites with regard to the flare site on 2012 March 10. (B) White-light CME observed by the SOHO/LASCO C2 coronagraph. (C) Enlarged disk-view of this event from SDO/AIA 171 Å. The flare site is marked by a white box in (B). (D) Limb-view of this event from STEREO-A/EUVI 171 Å.

After a brief description of the VLA in Section 2.1 and an overview of the flare context in Section 2.2, we discuss VLA radio imaging spectroscopic observations in Section 2.3. In Section 2.4, we present 3D reconstruction of the flare arcades observed in radio, EUV, and X-rays to elucidate the location of the spike bursts above the looptops. We also show evidence of the presence of a supra-arcade fan and downflows in the close vicinity of the spike bursts. We discuss and briefly summarize our findings in Section 3.

2. OBSERVATIONS

2.1. *Karl G. Jansky Very Large Array*

The VLA is a general-purpose radio telescope array which completed a major upgrade in 2011 (Perley et al. 2011). The full VLA array consists of 27 antennas, each of which has a diameter of 25 m. The VLA was partially commissioned in late 2011 to enable solar observing with broadband dynamic spectroscopic imaging (Chen et al. 2013). It allows radio images to be made at >1000 simultaneous frequency channels at an ultra-high time cadence of up to 10 ms for each circular polarization. At the time of this study, the VLA was commissioned for solar observing at its L (1–2 GHz), S (2–4 GHz), and C (4–8 GHz) bands. Recently, support for solar observing was expanded to also include the P (0.23–0.47 GHz), X (8–12 GHz), and Ku (12–18 GHz) bands. Recent studies with the VLA have demonstrated its unique power in utilizing a variety of coherent radio bursts, including type III radio bursts, fiber bursts, and spike bursts, and incoherent gyrosynchrotron bursts to trace flare-accelerated electrons in the close vicinity of the energy release site (Chen et al. 2013, 2014, 2015, 2018, 2019; Wang et al. 2017; Yu & Chen 2019; Sharma et al. 2020).

2.2. *Event Overview*

The event under study is a GOES-class M8.4 eruptive flare occurred on 2012 March 10 located in AR 11429. The standard identification ID for this event is SOL2012-03-10T17:14:40L280C090 following the IAU convention (Leibacher et al. 2010).

This AR is a highly flare-productive region, which hosted more than ten >M-class flares (including three X-class flares) and coronal mass ejections (CMEs) from 2012 March 2 to 17. Several studies reported the magnetic structure and evolution of this AR, as well as their relation to the flare/CME activities (Elmhamdi et al. 2014; Chintzoglou et al. 2015; Zheng et al. 2017). Successive eruptions and white light CMEs from this AR were reported spanning almost the entire duration when the AR was visible from Earth (Chen et al. 2014; Liu et al. 2014; Wang et al. 2014; Chintzoglou et al. 2015; Dhakal et al. 2018, 2020), some of which were accompanied with shock waves (Magdalenić et al. 2014), solar energetic particle (SEP) events (Kouloumvakos et al. 2016), and high-energy gamma-ray emission (Ajello et al. 2014). This AR is also of special interest for space weather related studies. In particular, the two X-class flares on 2012 March 7, accompanied by

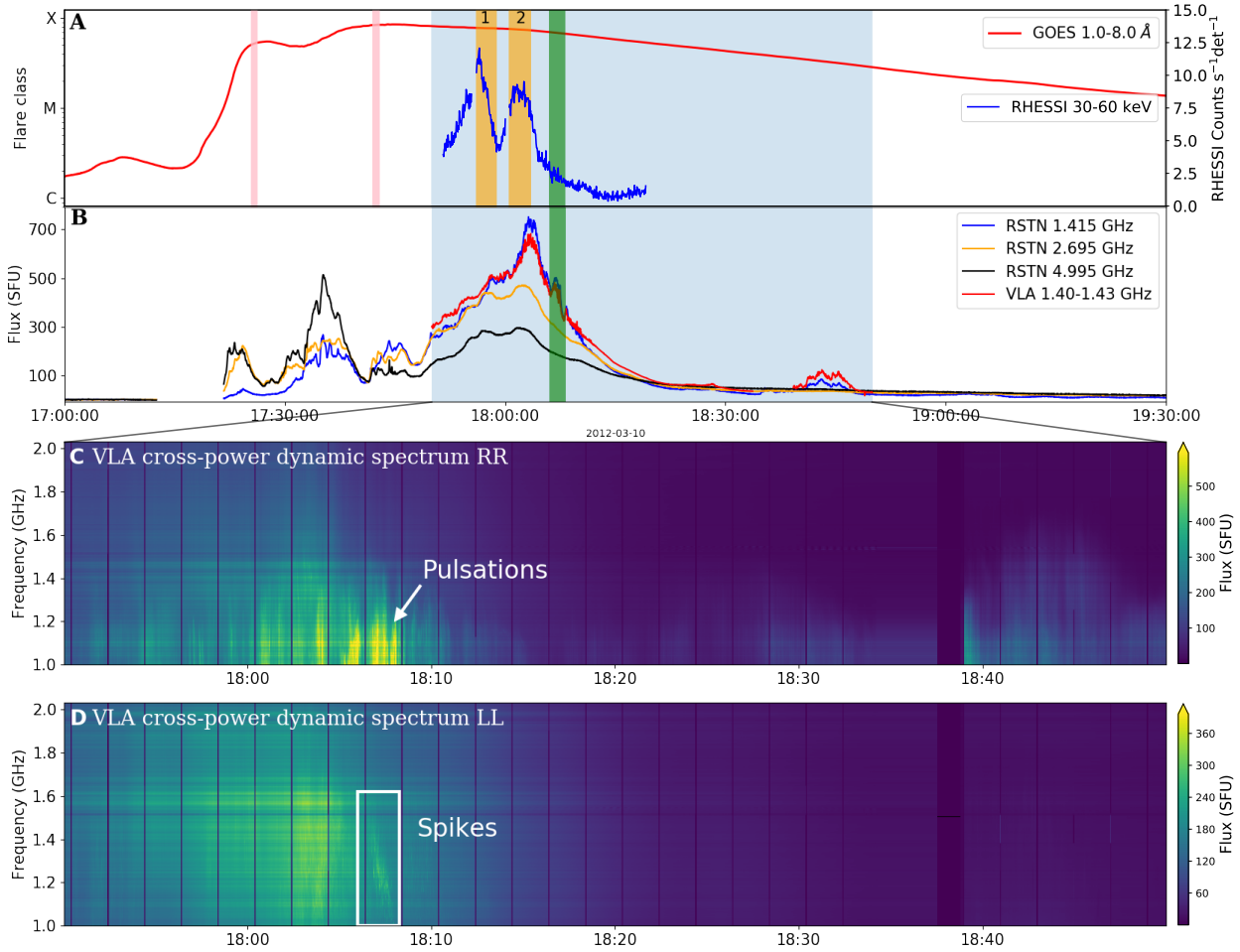

Figure 2. Radio and X-ray light curves of the SOL2012-03-10T17:14:40L280C090 M8.4 eruptive solar flare event. (A) RHESSI 30–60 keV (blue), GOES 1.0–8.0 Å (red) light curves. Two pink vertical lines represent the two soft X-ray peaks at ∼17:26 UT and ∼17:42 UT, respectively. The orange shadowed area represents the two time intervals (marked with "1" and "2", 17:56:08 UT - 17:58:54 UT for interval 1, 18:00:35 UT - 18:03:33 UT for interval 2, respectively) used in producing the RHESSI images shown in Figs. 4 and 7. The green shaded area represents the period when the spike bursts are present. (B) Light curves from the Radio Solar Telescope Network (RSTN) pre-flare background-subtracted total solar flux at 1.415 GHz (blue), RSTN 2.695 GHz (orange), RSTN 4.995 (black), and VLA 1.40-1.43 GHz (red). (C) and (D) VLA radio cross-power dynamic spectra in RCP and LCP, respectively. The VLA cross-power dynamic spectra and light curve are obtained from a short baseline with a length of 181 m. The duration of the dynamic spectra is indicated by the light-blue-shaded region in panels (A)–(B). The spike bursts of interest are marked by a white box in (D).

two ultra-fast (>2,000 km s^{-1}) CMEs, led to one of the largest geomagnetic storm of solar cycle 24 (Patsourakos et al. 2016).

The M8.4-class eruptive flare event under study was observed by the Atmospheric Imaging Assembly (AIA; Lemen et al. 2012) aboard the Solar Dynamics Observatory (SDO; Pesnell et al. 2012) at multiple EUV bands against the disk (Figure 1(C)). One of the STEREO satellites (*STEREO-A*) also observed this event (Figure 1(D)). The spacecraft was located at 109.5° west from Earth at the time of the observation (Figure 1(A)), and had an almost perfect limb view of this event (Figure 1(D)). The two EUV imagers combined thus provided a unique view of the flare event from two different vantage points at the same time.

By utilizing both *SDO*/AIA and *STEREO-A*/EUVI observations, Dhakal et al. (2018) studied the 2012 March 10 M8.4 event in detail. They concluded that the event was driven by a "compound" eruption of two filaments with a "double-decker" configuration. In Section 2.4, we will discuss our three-dimensional reconstruction of the flare loops within the eruption context set forth in their study.

The GOES 1–8 Å soft X-ray (SXR) flux started to increase at ∼17:15 UT. The light curve had two peaks, one at ∼17:26 UT and another at ∼17:42 UT (Figure 2(A); see also Dhakal et al. 2018). This flare is located at 17° north and 24° west (in Heliographic longitude and latitude, respectively, or N17W24) on the solar disk. It was associated with a fast white-light halo coronal mass ejection (CME; Figure 1(B)) whose speed exceeded 1200 km s^{-1}.

VLA observed this flare event from 17:46:18 UT to 21:46:46 UT in its C configuration with 15 antennas. The longest baseline is 2,669 m (which corresponds to an angular resolution of ∼19″ at 1.5 GHz). The observation was made in both right- and left-hand circular polarizations (RCP and LCP) in the 1–2 GHz L band. The frequency band was divided into 8 independent spectral windows, each of which had 128 1-MHz-wide spectral channels. Therefore, it provided spectroscopic imaging at a total of 1024 independent frequency channels simultaneously with a time cadence of 50 ms. Flux, bandpass, and delay calibration were performed against 3C48, and antenna gain calibration was performed against J2130+0502, both of which are standard celestial calibrator sources for VLA. 20 dB attenuators are inserted in the signal path during solar scans to reduce the antenna gain, and corresponding corrections in phase and amplitude were made to the data (Chen et al. 2013).

A rich variety of decimetic radio bursts were observed by the VLA during the entire duration of its 4-hr observing, which included broadband continuum emission, zebra-pattern bursts, fiber bursts, pulsations, and spike bursts. Figures 2(C) and (D) show the VLA cross-power radio dynamic spectra (from one short baseline with a length of 181 m) from 17:50 UT to 18:50 UT in RCP and LCP, respectively. The stochastic spike bursts were observed at around 18:07 UT during the extended energy release phase, ∼5 minutes after the HXR peak at 18:02 UT (green vertical bar in Figures 1(A) and (B) and white box in Figure 1(D)). In the following section, we will investigate these spike bursts in detail by utilizing radio dynamic spectroscopic imaging, and suggest that they are likely associated with a flare termination shock in this event, similar as that reported in Chen15.

2.3. *Radio Imaging Spectroscopy*

Around the time of interest when the spike bursts are present (∼18:07 UT), radio imaging in our observing frequency range shows three distinct sources (Figure 3(A)). One source is located close to the east flare ribbon (Source I; blue contours). Another source is located at the top of the flare arcades (Source II; orange contours). A third source is located ∼70″ away from the looptop source toward the west (Source III; red contours). VLA's capability of radio dynamic spectroscopy imaging allows us to image every pixel in the time-frequency domain, resulting in a time-series of 3D spectral image cubes (two in space, one in frequency) in each polarization product. Such essentially 4D spectrotemporal image cube can be used to generate a spatially-resolved, or "vector" dynamic spectrum, from any selected spatial region of interest, thereby elucidating the spectrotemporal properties intrinsic to the given source (e.g., Chen et al. 2015, 2018; Mohan & Oberoi 2017; Yu & Chen 2019). We employ this technique to produce a vector dynamic spectrum for each of the three radio sources, shown in Figures 3(B), (C), and (D), respectively. The vector dynamic spectra for the three sources are strikingly different: Source I displays highly polarized bright pulsating signatures with many complex fine structures, with a peak brightness temperature (T_B) of over 10^{10} K. The pulsation source is possibly due to coherent radiation by trapped energetic electrons (see, e.g., Carley et al. 2019), which may be the topic of a future study. Source II at the looptop, in contrast, is a weakly polarized, continuum-like emission, which has a brightness temperature that increases in frequency to about 10^9 K. Source III, which is the focus of the current study, shows a large group of short-lived, narrow-bandwidth spike bursts. The dynamic spectral features of this source closely resemble the stochastic spike burst event reported in Chen15, who attributed them as radio signature of emission at myriad density fluctuations at or close to the flare termination shock front. The spike bursts are highly polarized in LCP, and have a peak T_B of over 10^9 K.

2.3.1. *Looptop Continuum Source*

The rising spectrum of the looptop continuum source (Source II in Figure 3) in 1–2 GHz is consistent with the spectral characteristics of the optically thick portion of gyrosynchrotron radiation at the same frequency range (e.g., Dulk & Marsh 1982). To further confirm the gyrosynchrotron nature of the looptop continuum source, we utilize concurrent total-power data obtained by the Radio Solar Telescope Network (RSTN) at eight discrete frequencies: 0.245 GHz, 0.410 GHz, 0.610 GHz, 1.415 GHz, 2.695 GHz, 4.995 GHz, 8.800 GHz, and 15.40 GHz. The RSTN flux for the lowest three frequencies (below 1 GHz) reached over 1,000 solar flux unit (SFU) at ∼17:57, and have very different temporal behavior from their higher frequency counterparts. They are likely dominated by coherent emission. Also as VLA covers the 1.415 GHz band, RSTN fluxes at the

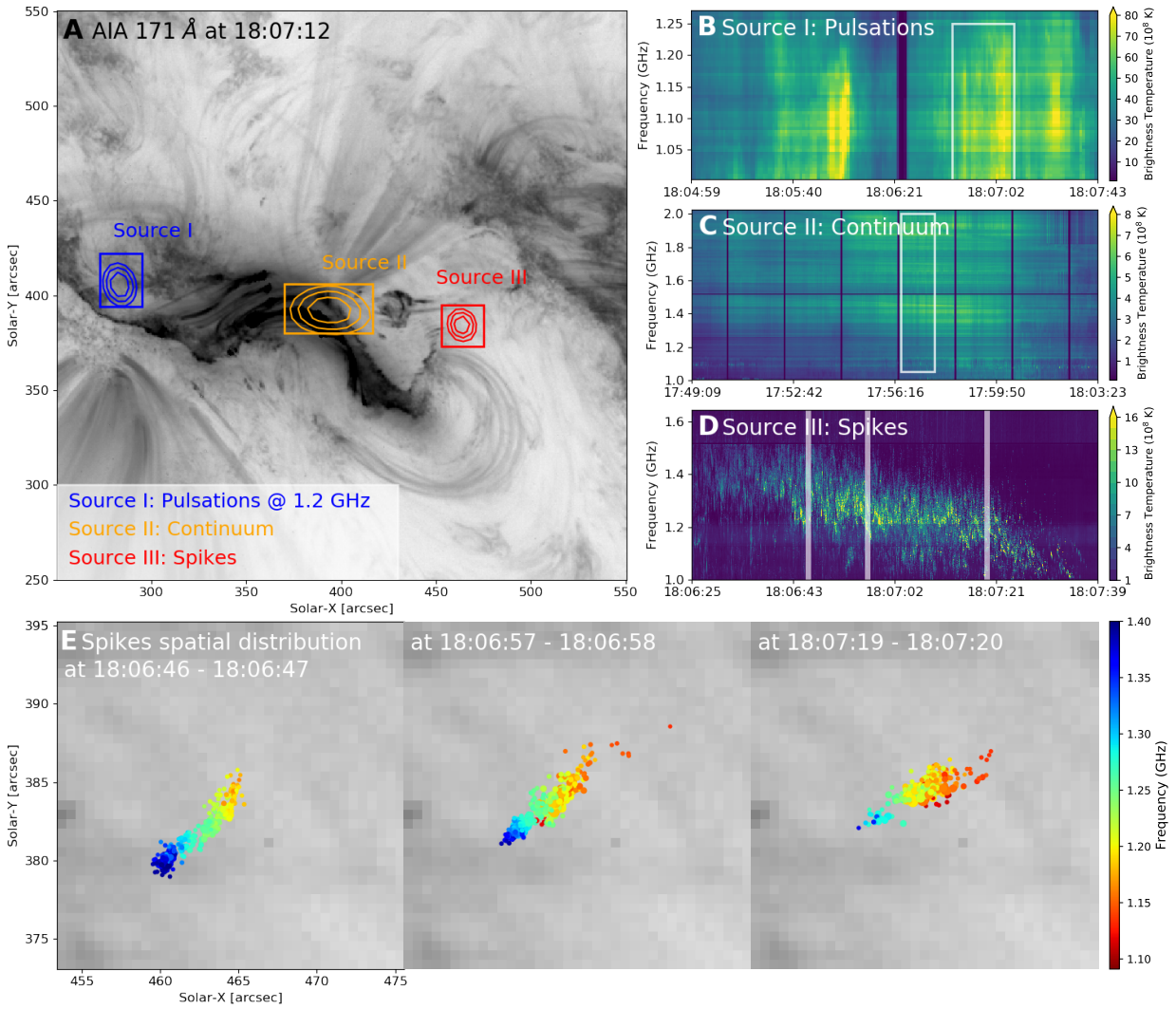

Figure 3. VLA dynamic spectroscopic imaging of different radio sources during the extended energy release phase of the flare. (A) Radio images for the three sources near the time of the spike bursts shown as contours in different colors (contour levels are 70, 80 and 90% of the maximum). Background (inverted grayscale) image is SDO/AIA 171 Å. (B)–(D) Spatially-resolved vector radio dynamic spectra associated with the pulsation source located near the east flare ribbon (Source I; shown in RCP), the looptop continuum source (Source II; shown in Stokes I) and the stochastic spike source (Source III; shown in LCP), respectively. White boxes in (B) and (C) indicate the time and frequency range of the corresponding radio images (Sources I and II) shown in (A). For Source III, the image shown is made by taking a 70 s integration (18:06:25 UT to 18:07:35 UT) in 1.0–1.5 GHz. (E) Distributions of the centroid locations of all the spike bursts (Source III) within each of the three selected 1-s periods (indicated by vertical shades in (D)). Red to blue indicate increasing frequencies. The field of view is the same as the red box in (A). An accompanying animation is available online. The left panel of the animation is the vector dynamic spectrum identical to panel (D), with a vertical strip indicating the corresponding time. The right panel of the animation shows the ensemble of the spike centroids from 18:06:25 to 18:07:25 UT similar to the snapshots in panel (E). The duration of the animation is 7 s.

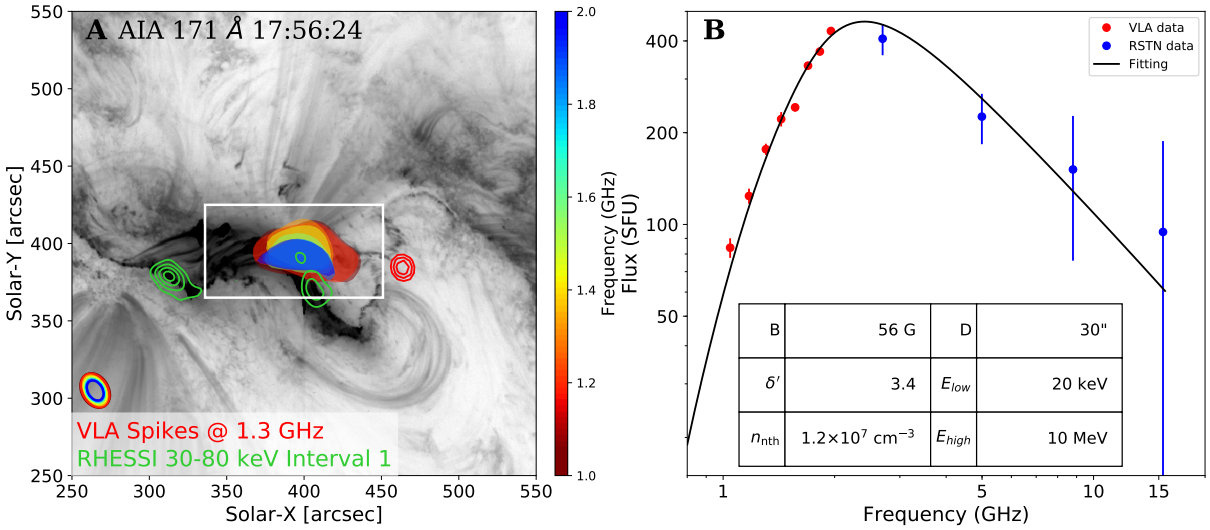

Figure 4. Imaging spectroscopy of the looptop radio continuum source (Source II in Fig. 3) and gyrosynchrotron fitting results. (A) Spectral-resolved contours of the looptop radio continuum source at each spectral window (50% of the maximum brightness temperature at its frequency in looptop area). Color from red to blue indicates increasing frequency (see color bar on the right). The corresponding FHWM beam sizes are shown on the left bottom. Green contours are RHESSI 30–80 keV HXR footpoint sources (HXR interval 1 in Figure 2(A), 17:56:08 UT to 17:58:54 UT) that coincide with the double flare ribbons. (B) Radio flux density spectrum of the looptop radio continuum source and gyrosynchrotron fitting results. VLA measurements, shown as red dots, are derived by summing all the fluxes within white box in (A). Blue dots are total-power data observed by RSTN at 2.695, 4.995, 8.8 and 15.4 GHz.

lowest four frequencies are excluded from the subsequent analysis.

To enable direct comparison to the spatially-resolved VLA observations of the looptop source, first, we subtract the post-flare background at ∼19:30 from the observed RSTN flux at 17:57 to remove the contribution from the quiescent solar disk and active region. Background-subtraction is also performed on VLA data at 17:57 by selecting the same post-flare time as the background in looptop region (white box in Figure 4(A)). Second, we take the assumption that the radio emission above 2 GHz is dominated by the looptop source. This assumption is mostly valid, as VLA imaging reveals that the looptop source plays a dominant role at above ∼1.4 GHz (c.f., Figure 2) during the time of interest. Uncertainties of flux values derived from VLA data are estimated by using the root mean square (RMS) variations of a region in the image without the presence of any source. For the uncertainty estimates for RSTN-derived flux values, we take the RMS variations of the measured total flux during a non-flaring time.

The resulting spectrum of the looptop source is shown in Figure 4(B). With the addition of RSTN flux at higher frequencies (>2 GHz), the spectrum shows features characteristic of nonthermal gyrosynchrotron radiation, with a positive and negative slope at the low- and high-frequency side (due to optically thick and thin emission, respectively) and a peak flux of ∼400 SFU. Although the combined microwave spectrum does not allow us to accurately determine the source parameters owing to the assumptions taken above and the lack of spatial resolution across the spectrum, for demonstration purposes, we perform spectral fitting based on a homogeneous source model by adopting the fast gyrosynchrotron codes in Fleishman & Kuznetsov (2010) to calculate the gyrosynchrotron spectrum. An example fit result and the associated source parameters are shown in Figure 4(B)[1]. Although the fit parameters are subjected to the limitations noted above and are probably not unique, our analysis demonstrates that the looptop continuum source is most likely due to the incoherent gyrosynchrotron emission from flare-accelerated nonthermal electrons.

2.3.2. *Stochastic Spike Source*

As mentioned earlier, the vector dynamic spectral features of Source III closely resemble the stochastic spike burst event reported in Chen15. The group of spike bursts lasted for around 70 seconds from 18:06:25 to 18:07:35 UT in the frequency range of 1.0–1.6 GHz. It contains a total of over 10,000 individual bursts within the ∼70-s duration. Similar to the spike bursts reported by Chen15, the bursts are extremely short-lived—most are unresolved by the time resolution of the instrument 50 ms—and have a narrow bandwidth $\delta\nu/\nu$ of only a few percent.

To further study the spectral properties of the spike bursts, we adopt the same technique described in Chen15 to perform a multi-Gaussian fit of the spectral profiles of the spike bursts at each time integration. To reduce the noise in the spectral domain and achieve more robust fit results, we have smoothed the spectral profiles with a 6-MHz-wide boxcar window. Further, in order to limit our fitting to sufficiently bright spike bursts, we have also applied a brightness threshold of $T_B^{\rm min} = 0.7 \times 10^8$ K, set as about 4 times of the RMS variations of a region in the image without any source. The fitting range of the spike bandwidth (represented by the full-width-half-maximum, or FWHM, of the Gaussian profiles) is limited to 6–100 MHz. Typical examples of the fit results for three selected times are shown in Figure 5(A). From the multi-Gaussian fitting results we obtain a distribution of the spike bandwidth, shown as a histogram in Figure 5(B). Similar to the bandwidth distribution of the spike burst event shown in Chen15 (their Figure S3 in Supplementary Materials), the spikes have an asymmetric distribution that peaks at 22 MHz (or a relative bandwidth $\delta\nu/\nu \approx 2\%$, density fluctuation $\delta n_e/n_e \approx 4\%$). The brightness temperature distribution is also notably similar to that shown in Chen15. We note that, however, the maximum brightness temperature is two orders of magnitude greater than that reported in Chen15. It can be possibly attributed to the much larger flare (M8.4 vs. C1.9) in which our spike bursts are observed (see, e.g., Benz et al. 2005, who reported that coherent radio bursts are generally brighter in larger flares), yet the underlying relationship is highly complex, which involves many factors including flare timing, shock generation, electron acceleration, and the coherent radiation processes. Nevertheless, the very similar spectrotemporal properties to those reported in Chen15 suggest that the spike bursts are likely associated with the same emission processes.

We further derive the centroid location of the radio source at each time and frequency pixel where the spike burst is present by using a 2D polynomial fitting technique following Chen15. The 2D polynomial fitting utilizes the 6 pixels surrounding the pixel where the maximum brightness is located to perform second-order poly-

[1] Source parameters listed in Figure 4(B) are: magnetic field strength B, power-law index δ' of the electron density distribution, total nonthermal electron number density $n_{\rm nth}$, low- and high-energy cutoff of the power-law nonthermal electron distribution $E_{\rm low}$ and $E_{\rm high}$, and column depth D.

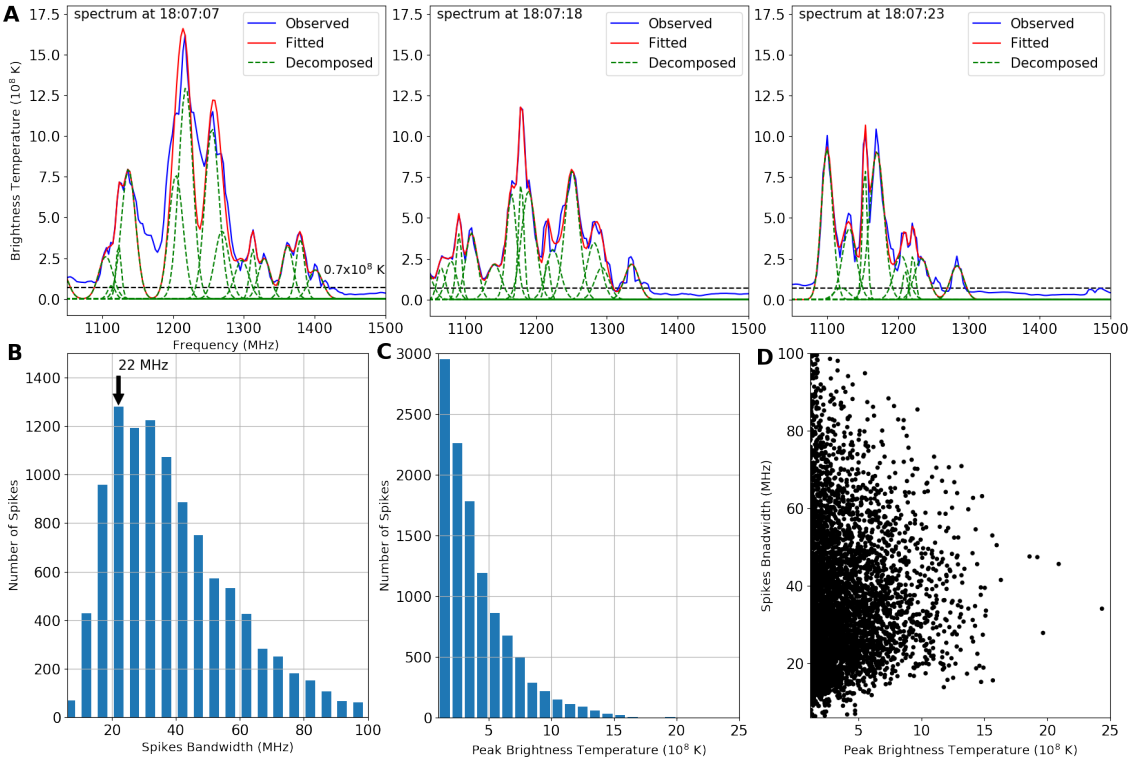

Figure 5. Spectral characteristics of spikes. (A) Examples of multi-Gaussian spectral fitting results for the VLA radio spectra at three different times. Blue and red solid lines are the observed and fitted spectra. Green dashed curves are the multiple Gaussian components used in the fitting. The T_B threshold adopted for the fitting is indicated by a horizontal dashed line. (B, C) Bandwidth and peak brightness temperature distribution of the spikes from the fitting results. (D) Scatter plot of the peak brightness temperature versus bandwidth of the spikes.

nomial fitting in two orthogonal directions. The location of each source centroid is found at the peak of the polynomial curves. The uncertainty of the resulting centroid position is estimated by $\sigma \approx \theta_{\rm FWHM}/({\rm S/R}\sqrt{8\ln 2})$ (Reid et al. 1988; Condon 1997; Chen et al. 2015, 2018), where the signal to noise ratio S/R is the ratio of the peak flux to the root mean square noise of the synthesized image where a source is not present, and $\theta_{\rm FWHM}$ is the full-width half maximum of the synthesized beam. With the $\theta_{\rm FWHM} = 19.9'' \times 14.6''$ at 1.6 GHz and typical S/R values greater than 40, the accuracy of our derived source centroid position is typically better than $1''$.

As shown in Figure 3(E), at any given time, the derived centroid locations of the spike bursts at different frequencies form a nearly linear feature with a length of about $10''$. This distinctive feature shows some temporal evolution, and lasts for about 70 seconds before it diminishes at 18:07:35 UT (see Figure 3(E) for snapshots at three different times and the associated animation). This feature shows a slight overall movement toward the southwest direction (or a movement toward the lower-right corner in Figure 3), which corresponds to a gradual overall frequency drift of the spike burst group toward lower frequencies in the dynamic spectrum (Figure 3(D)). The observed features closely resemble the findings in Chen15, who interpreted the feature as the projection of a presumably 3D termination shock front above the flare arcades, and the overall frequency drift as the movement of the shock front in the looptop region with a varying plasma density. We note that, however, unlike the event reported in Chen15 and Chen19, this event does not show any sign of sudden disruption of the feature nor a split-band feature.

Although VLA radio imaging shows that the spike source is located away from the flare arcades, as expected from the termination shock scenario in which the shock front is situated above the looptops, it is not immediately clear if the exact location and orientation of the spike source are consistent with the termination shock interpretation. In the next two subsections, we will take advantage of the concurrent observations obtained by both *SDO*/AIA and *STEREO-A*/EUVI from two vantage viewing points, and establish its spatial relation between the eruption, the flare arcades, as well as the supra-arcade fan and downflow structures.

2.4. *Spike Source Location in a 3D Context*

Unlike the stochastic spike burst event reported in Chen15 which had a limb-view, the spike source under study here is observed against the disk. Therefore, the projection effect renders our interpretation for the spike source in the flare context not as straightforward as the limb event. Fortuitously, as reported by Dhakal et al. (2018), the event was recorded simultaneously by *SDO*/AIA and *STEREO-A*/EUVI from two viewing perspectives: *SDO* viewed it against the disk and *STEREO-A* viewed the eruption from the limb (panels (A) and (C) in Figure 6, respectively). These observations give us a unique opportunity for understanding the location of the radio sources in a three-dimensional flare context. In this subsection, we will first reconstruct the geometry of the erupting filament and flare arcades using observations from two vintage viewing perspectives. We will then place the observed spike bursts, looptop gyrosynchrotron radio source, and SXR source in the physical context of this eruptive flare.

2.4.1. *Erupting Filament*

In Dhakal et al. (2018), by using both *SDO*/AIA and *STEREO-A*/EUVI observations, the authors suggested that the event was driven by two pre-existing filaments with a "double-decker" configuration. As observed by *SDO*/AIA, the filaments were formed prior to the flare along the primary polarity inversion line (PIL; red curve in Figure 6) with a northeast-southwest orientation. The double-decker filaments erupted successively ∼12 minutes apart prior to the second GOES SXR derivative peak at ∼17:37 UT. After ∼17:30 UT, the two erupting filaments merged together and became nearly indistinguishable from each other. The erupting filament, seen in *SDO*/AIA 304 Å has a writhed shape and directs towards the northwest (Figure 6(B)). The eruption is less evident in *SDO*/AIA 131 Å images, but can be distinguished using the running-difference imaging technique (Figure 6(A)). This passband is sensitive to a much higher temperature (∼10 MK) associated with the Fe XXI line (O'Dwyer et al. 2010), which is presumably emitted by the hot envelop of the magnetic flux rope encompassing (and likely above) the cool filament (e.g., Chen et al. 2014; Cheng et al. 2014). Similar to Dhakal et al. (2018), we track the eruption front seen in *SDO*/AIA 131 Å, shown as blue dashed lines in Figure 6(A). In *STEREO-A*/EUVI's limb view, the erupting filament clearly displays a writhed morphology (Figure 6(C)), which strongly suggests that it is a magnetic flux rope in nature (e.g., Ji et al. 2003; Török & Kliem 2005) and is consistent with the morphology of the filament viewed from *SDO*/AIA.

The conjugate ends of the eruption coincide with two coronal dimming regions in *SDO*/AIA 211 Å base-difference images (difference of the post- and pre-flare intensity; orange patches in Figure 6) located at the opposite sides of the PIL. These twin coronal dimmings, often observed during the eruption phase of CME-associated events in EUV and SXR, have been interpreted as density depletions at the conjugate ends of the expelled magnetic flux rope (e.g., Sterling & Hudson 1997; Zarro et al. 1999; Miklenic et al. 2011; Cheng & Qiu 2016). Their presence further supports the flux rope nature of the erupting filament.

2.4.2. *Flare Arcades*

The appearance of the flare arcades, as viewed by *SDO*/AIA and *STEREO-A*/EUVI, are consistent with the geometry of the erupting filament (Figure. 7). In *SDO*/AIA's view, the post-flare arcades are distributed from northeast to southwest, rooted at either sides of the preflare filament (Figure 7, middle column). In *STEREO-A*/EUVI's limb view, the same post-flare arcade system is projected to distribute in north-south direction along the limb, which is consistent with the geometry of the filament that erupted early on (Figure 7, right column). According to the standard picture of eruptive solar flares in three dimensions (Aulanier et al. 2012, 2013; Janvier et al. 2013, 2014, 2015), a large-scale reconnection current sheet is present below the erupting filament and above the post-flare arcade, driving the flare energy release and particle acceleration (see, e.g., a recent study by Chen et al. 2020a).

During the flare energy release phase, magnetic reconnection is likely patchy and intermittent (e.g., Aschwanden 2002). At any given time, reconnection occurs within a localized region, forming a newly reconnected flare arcade. Downward-propagating nonthermal electrons propagate along the legs of the flare arcade and produce a pair of compact HXR sources at the conjugate footpoints of the flare arcade as they bombard the dense chromosphere. Chromospheric material heated by the electron beams and/or thermal conduction at different times forms the observed flare ribbons at (E)UV and/or white light wavelengths, which are usually much more extended than the HXR footpoints source due to their much slower decay (see, e.g., discussions in Fletcher 2009; Qiu et al. 2010).

In our event, *RHESSI* 30–80 keV images made during the extended energy release phase (green and blue contours in Figures 7(A), (D), and (G), which correspond to the two intervals we selected for imaging shown in the light curve in Figure 2(A)) reveal multiple pairs of conjugate HXR footpoint sources distributed along the double

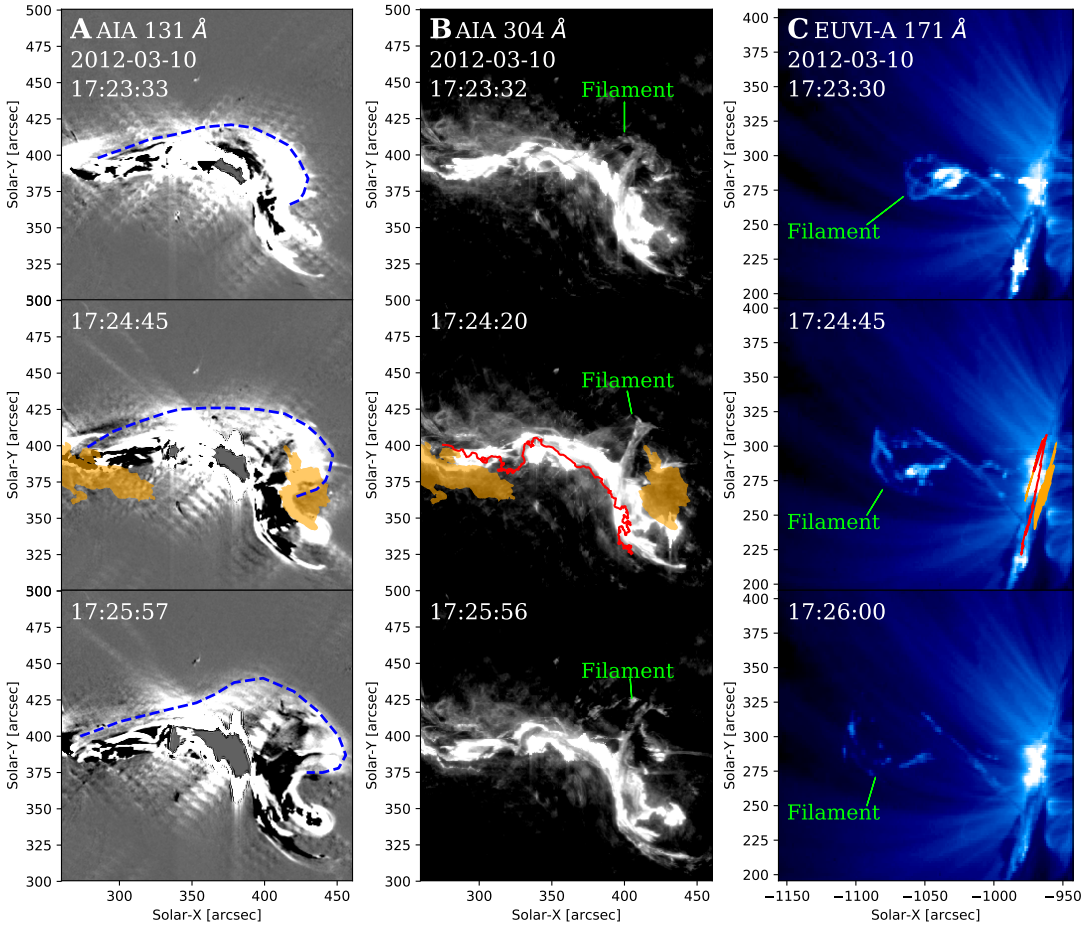

Figure 6. Erupting filament structure observed by *SDO*/AIA 131 (panel (A)), 304 Å (panel (B)), and STEREO-A/EUVI 171 Å (panel (C)) from two viewing perspectives. (A) *SDO*/AIA 131 Å running difference images, with the blue dashed curves represent the eruption front. The polarity inversion line (PIL) is shown as a red curve in panels (B) and (C). Orange patches represent the coronal dimming region detected from *SDO*/AIA 211 Å base-difference image (post-flare vs. pre-flare), which coincide with the ends of the eruption on opposite sides of the PIL. The orange patches in (C) are the same dimming regions transformed to *STEREO-A*/EUVI's perspective.

flare ribbons. The latter is clearly visible in *SDO*/AIA 1600 Å images (inverse grayscale background in Figure 7). The location and morphology of the HXR footpoints and UV flare ribbons are consistent with the standard flare scenario discussed above. The flare arcade itself is filled with flare-heated plasma, producing thermal SXR emission (*RHESSI* 12–15 keV; magenta contours in Figure 7(E)). X-ray spectral analysis using the `OSPEX` package available in `SolarSoft IDL` suggests a volume emission measure of 7.8×10^{48} cm^{-3} and a temperature of 19 MK (Appendix A). Flare-accelerated electrons are often trapped at or above the top of the flare arcade, producing (above) looptop HXR and/or radio sources (e.g., Gary et al. 2018; Chen et al. 2020b). In this event, as already discussed in Section 2.3, such a looptop radio source is also present, likely due to gyrosynchrotron radiation from flare-accelerated nonthermal electrons. A looptop HXR counterpart is not detected by *RHESSI*. We attribute such a nondetection to its limited dynamic range for imaging the presumably weak coronal source in the presence of strong footpoint HXR sources (e.g., Krucker et al. 2008).

Both the RHESSI 12–15 keV SXR source and VLA gyrosynchrotron radio source display an arcade shape. We adopt a semi-ellipse 3D loop modeling approach to match the morphology of the observed SXR and radio arcade, using the HXR footpoint sources and bright UV flare ribbon kernels as their anchoring points. Free parameters in the 3D loop model include the major and minor axis of the ellipse a and b (with their ratio $e = a/b$), the inclination angle α of the ellipse plane about the plane perpendicular to the solar surface (a positive an-

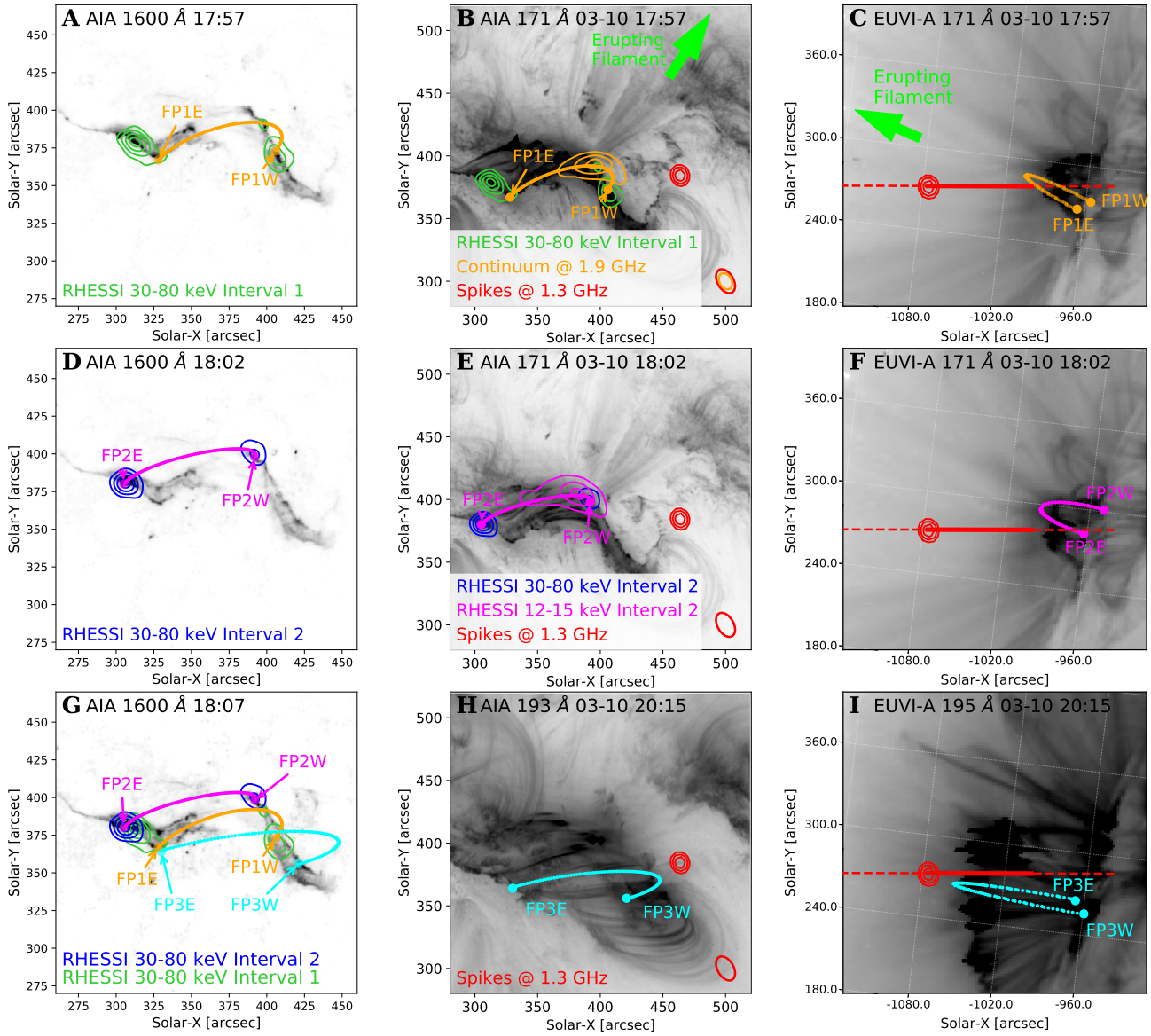

Figure 7. 3D reconstruction of flare arcades. (A) and (D) *RHESSI* 30–80 keV footpoint sources at intervals 1 and 2 (17:56:08 UT– 17:58:54 UT and 18:00:35 UT–18:03:33 UT, respectively) and the concurrent *SDO*/AIA 1600 Å images shown in inverted grayscale. (B) and (C) 3D reconstructed loop (thick orange curve) that connects the footpoint sources and the VLA looptop radio continuum source (orange contours) in *SDO* and *STEREO-A*'s view. Green arrows illustrate the direction of the erupting filament (c.f., Fig. 6). The spike burst is shown as red contours in (B). (E) and (F) are similar to (B) and (C) but instead show the 3D reconstructed loop (thick magenta curve) based on the SXR arcade (magenta contours) and the HXR footpoints (blue contours) in interval 2. The line of sight of an Earth-based observer passing the spike source in *STEREO-A*'s view is shown as a red dashed line. The solid portion shows the range of the possible spike source location above the apex of the transformed SXR arcade, with its best-estimate shown as the red contours. (G) Similar to (A) and (D) but includes a reconstructed post-flare arcade in *SDO*/AIA 193 Å and *STEREO-A*/EUVI 195 Å images at about 2 hr later (cyan curve). The latter is shown in (H) and (I). The size of the synthesized beam is shown in the bottom right corner.

gle means a northward inclination), as well as the rotation angle θ of the ellipse about its center ($\theta = 0°$ corresponds to a ellipse with its vertices coinciding with the HXR footpoints or bright ribbon kernels). The relation between the separation of the loop footpoints ($2l$) in terms of a, b, and θ is:

$$l^2 = a^2 b^2 / (b^2 \cos^2\theta + a^2 \sin^2\theta). \quad (1)$$

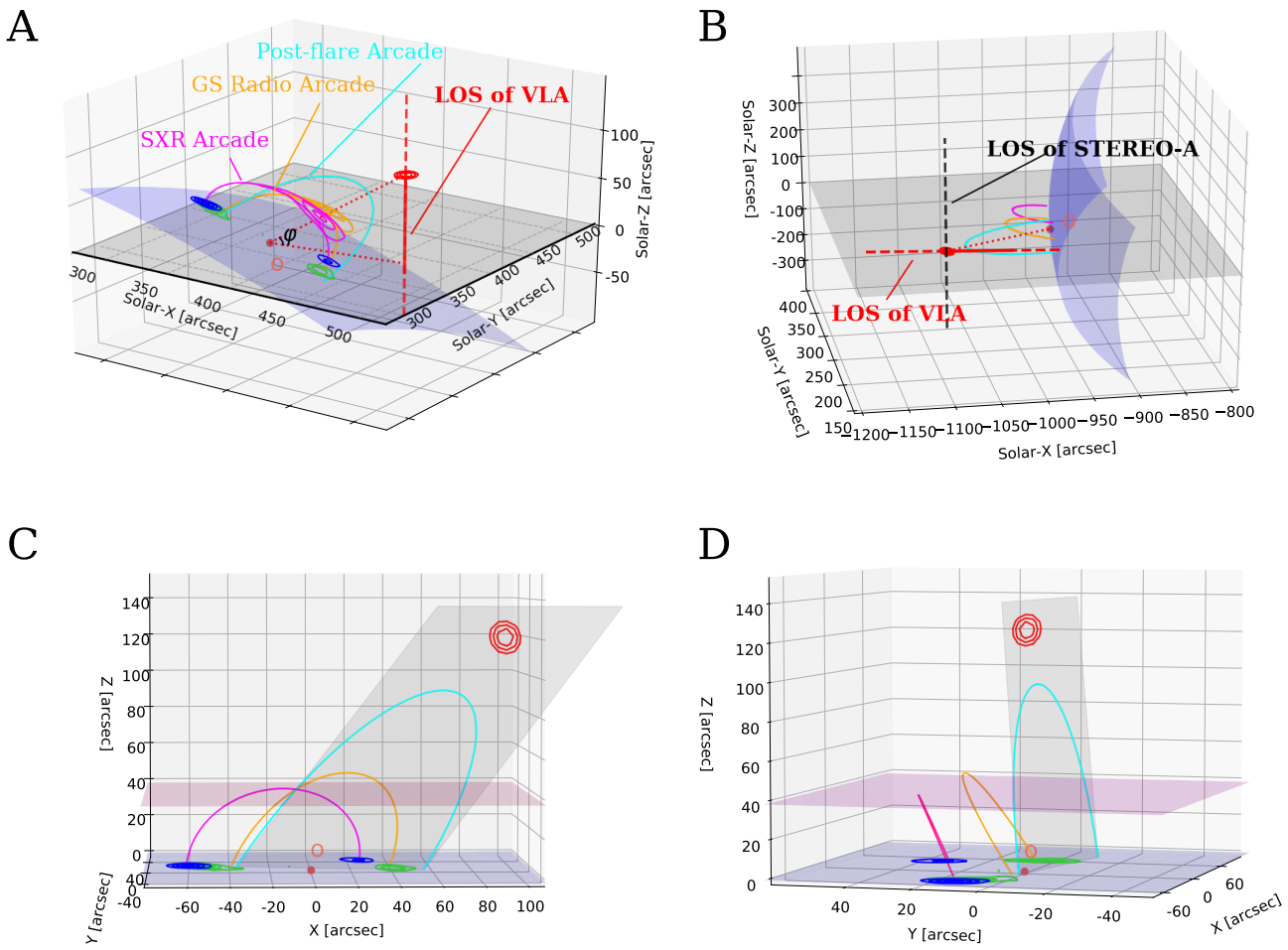

Figure 8. 3D view of the reconstructed loops. (A) and (B): Reconstructed loops in *SDO* and *STEREO-A*'s viewing perspective, respectively. They are identical to those in Figure 7: magenta, orange, and cyan curves are for the SXR arcade, GS radio arcade, and the post-flare arcade at 20:15 UT, respectively. The X–Y plane is the plane of the sky in each perspective. The Z-axis is the direction orthogonal to the X–Y plane, i.e., the line of sight of each viewing perspective. The blue curved surface represents the solar surface. The projection angle φ discussed in the text is defined as the angle between the line connecting the best-estimate of the spike source location (red contours) and the plane of the sky in *SDO*'s view. (C) and (D): Detailed view of the spike source with respect to the three reconstructed loops in a face-on and edge-on projection. The gray surface represents the plane of newly-reconnected arcade (cyan curve). The blue-shaded bottom plane is (approximately) the solar surface with the origin of the X-, Y-, and Z-coordinates located at the mid-point of the radio GS arcade (orange curve) marked as "o". The pink surface marks the radial height of the apex of the SXR arcade.

With l fixed using the observed footpoint separation, the remaining free parameters that defines the 3D semi-ellipse loop are $e = a/b$, the rotation angle θ, and the inclination angle α. We adjust these parameters until each loop model in projection (from Earth view) matches the morphology of the observed looptop radio and SXR arcade. The resulting best-fit semi-ellipse loops are shown as the thick orange and magenta curve in Figures 7(B) and (E), respectively. The same loop models are then projected from the viewing perspective of *STEREO-A*/EUVI (orange and magenta curves in Figures 7(C) and (F). We will refer to the two model arcades in which the gyrosynchrotron radio source and looptop SXR are situated, respectively, as the "GS radio arcade" and "SXR arcade" hereafter.

2.4.3. *Spike Source Location*

The spike source, as viewed from Earth by the VLA, is located ∼70″ westward in projection from the top of the GS radio arcade (Figure 7(B)). Unlike the looptop SXR and GS radio sources that have an arcade-like shape, the spike source is unresolved (the synthesized beam is

shown in all panels of Figure 7 in the center column as an ellipse). Therefore, the same loop modeling technique described previously can not be applied to constrain its 3D geometry. Without further constraints, the spike source can, in principle, be located anywhere along the line of sight (LOS) of VLA, shown as a red dashed line in STEREO-A's view in Figures 7 and 8. However, if we adopt the termination shock scenario, it is reasonable to assume that the spike source is located above the top of the flare arcade and makes the same projection angle φ as the looptop of the GS arcade, defined as the angle between the semi-minor axis of the semi-ellipse loop model for the GS radio arcade and the plane of the sky ($\varphi \approx 43°$; shown in Figure 8(A)). Therefore, a displacement of $d \approx 98''$ from the center of the semi-ellipse loop model for the GS radio arcade (marked as "o" in Figure 8(A)) to the spike source in projection, translates into an absolute distance $D = d/\cos\varphi \approx 134''$. Knowing the location of the spike source in 3D, we can then derive its (radial) height above the solar surface to be $h \approx 120'' \approx 86$ Mm. Adopting such a height, in *STEREO-A*/EUVI's view, we mark the inferred spike source location as red contours, located well above the top of the flare arcades. The plane defined by the inferred 3D location of the spike source and the conjugate HXR footpoints is close to the plane where the GS radio arcade is situated, but is tilted further toward solar south by ∼21°. If we apply the same method on the SXR arcade to estimate the spikes location, it gives a slight difference (∼5″) in the radial height of the spike source. Figure 8 visualizes the 3D spatial relation among the SXR arcade, GS radio arcade, and the location of the spike source from different viewing perspectives.

Our 3D reconstruction results place the best-estimate of the spike source location at about ∼120″ above the solar surface, or ∼60 Mm above the apex of the flare arcade. This is generally consistent with the termination shock scenario, in which a shock front is formed at the end of reconnection outflows above newly reconnected, cusp-shaped magnetic loops (see, e.g., MHD simulations in Chen15 and Shen et al. 2018). For this event, as viewed against the disk by *SDO*/AIA, these newly reconnected loops cannot be clearly distinguished due to the lack of column depth along the LOS. However, it is expected that they will relax and cool down to background coronal temperatures due to conductive and radiative cooling during the decay phase.

To look for signatures of loops formed around the time of the spike bursts, first, we use the formula given by Cargill et al. (1995) (their Equation (14E))

$$\tau_c = 0.0235 \frac{L^{5/6}}{(Tn)^{1/6}}, \tag{2}$$

where T and n are the initial temperature (in K) and density (in cm^{-3}) of a loop with a half-length L (cm), to estimate the loop cooling time. For a loop half-length of 10^{10} cm (or 100 Mm; estimated using the distance from the spike source to the center of the semi-ellipse model loop for the GS radio arcade D), and plasma temperature of 20 MK and density of 10^9–10^{10} cm^{-3} typical for flare-heated newly-reconnected loops, the loop cooling time τ_c is estimated as ∼2–3 hr. Using this cooling time as a guidance, in Figure 7, we show *SDO*/AIA 193 Å and *STEREO-A*/EUVI 195 images (differentially rotated back to 18:07 UT; the passbands are sensitive to 1–2 MK coronal plasma, see, e.g., Howard et al. 2008; O'Dwyer et al. 2010). In these images, we find multitudes of well-defined, cool postflare arcades. One representative semi-ellipse loop model that fits the observed AIA and EUVI arcade features is shown as the thick cyan curve in Figures 7(H) and (I). The apex of the loop is found to be present just below the best-estimate location of the spike source, which is consistent with the scenario of freshly reconnected loops located just beneath a termination shock front. We stress that the semi-elliptical EUV loops shown here may only represent the already relaxed (and cooled down) state of the reconnected loops after their shrinkage due to the magnetic tension force (e.g., Reeves et al. 2008). The newly reconnected loops themselves are usually observed to show a cusp shape when viewed from the side (e.g., Tsuneta et al. 1992; Tsuneta 1996), which are not visible in this event due to the unfavorable viewing perspective.

2.4.4. *Super-Arcade Fan and Downflows*

In the previous subsection, we have established that the spike source is likely located well above the flare arcades visible in radio, EUV, and SXR wavelengths and, possibly, just above freshly reconnected magnetic loops, which is consistent with the flare termination shock interpretation. Here we discuss another important piece of evidence that further supports this scenario: the presence of a supra-arcade fan and supra-arcade plasma downflows in the close vicinity of the spike source (or shock front). As shown in Figure 9, in *SDO*/AIA 131 Å (panel A) and *STEREO-A*/EUVI 195 Å (panel B) time-series images (both have sensitivity to 10–20 MK hot plasma; Howard et al. 2008; O'Dwyer et al. 2010, a long-lasting supra-arcade fan (SAF) structure is seen above the flare arcades from ∼17:50 UT to ∼19:30 UT. Similar to those previously reported in other eruptive events (Gallagher et al. 2002; Innes et al. 2014; Hanneman & Reeves 2014; Reeves et al. 2017, 2020; Cai et al. 2019), such SAF structures often have a diffuse appearance with many finger-shaped fine structures. Within

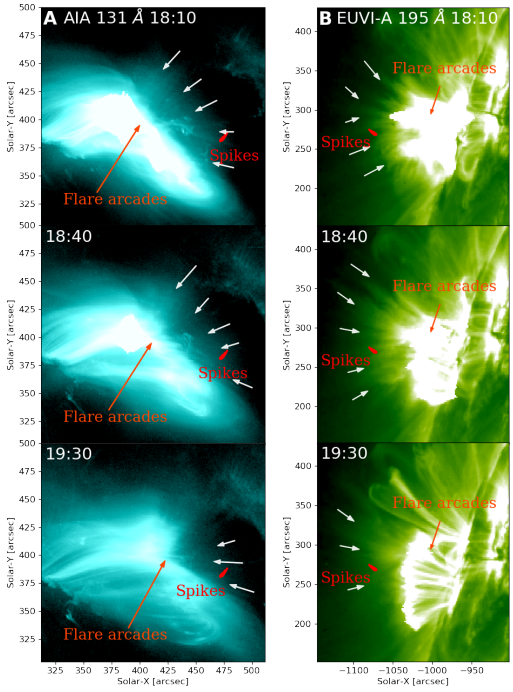

Figure 9. Supra-arcade fan (SAF) structure above the flare arcades. The SAF structure (marked as white arrows) is observed in both *SDO*/AIA 131 Å (panel A) and *STEREO-A*/EUVI 195 Å (panel B) images from ∼17:50 to ∼19:30 UT. The spike burst source at ∼18:07 UT is also shown. The location of the spike source in *STEREO-A*/EUVI's perspective is based on 3D reconstruction results discussed in Section 2.4.3. An animation of the dynamic SAF structure viewed from the two perspectives from 17:50 UT to 19:30 UT is available online. The duration of the animation is 3 s.

the SAF structure, multitudes of plasma downflows are identified at about 20 min after the time of the spike bursts. Figure 10(B) shows a clear example of a plasma downflow in *SDO*/AIA 131 Å time-series images appeared at around 18:25 UT. In the time–distance map of Figure 10(C), the speed of the downflow is found to be ∼166 km s^{-1} in projection, or ∼227 km s^{-1} if adopt the same projection angle of the looptop GS arcade $\varphi \approx 43°$.

Such a SAF structure is also clearly seen by *STEREO-A*/EUVI 195 Å with a limb-view perspective (Figure 9(B)). Based on our estimate of the 3D spatial location of the spike source discussed in the previous subsection, in Figure 9(B), we show the inferred location of the same spike source in the *STEREO-A*/EUVI 195 Å images by applying the same projection angle $\varphi \approx 43°$ for each spike centroid obtained at different frequencies. Similar to the spike location in *SDO*/AIA's view, the spike source is also located close to the top of the SAF structure. Several plasma downflow events are also identified in *STEREO-A*/EUVI 195 Å running-ratio images (intensity ratio of the current frame to the previous frame five minutes earlier) later into the event. Figure 11(B) shows an example of such a plasma downflow event at 19:00 UT. The apparent speed of the downflow is ∼53 km s^{-1} in projection. Such a speed appears much slower than those measured in *SDO*/AIA 131 Å images. However, we note that the low speed is most likely due to the selection bias: the low cadence of *STEREO-A*/EUVI 195 Å images (5 minutes, comparing to 12 seconds of *SDO*/AIA) only allows downflows with sufficiently slow speeds to be detected in consecutive frames.

3. DISCUSSIONS AND CONCLUSIONS

Here we have presented another stochastic spike burst event recorded by the VLA with radio dynamic imaging spectroscopy. The event was observed during the extended energy release phase of the SOL2012-03-10 M8.4 eruptive flare event, which is much stronger than the SOL2012-03-03 C1.9 event studied by Chen15. In VLA's vector dynamic spectrum, the spike bursts show very similar spectrotemporal features to those reported in Chen15, which consist of myriad highly polarized, narrow-band and short-lived spike bursts with a high radio brightness temperature of 10^9 K. VLA's dynamic spectroscopy imaging technique allows each frequency and time pixel in the dynamic spectrum to be imaged and the corresponding source centroid to be located with high accuracy (<1"). The centroids of the spike bursts at different frequencies delineate a nearly linear feature, located well above the bright EUV/X-ray flare arcade in *SDO*/AIA's view against the disk.

With the aid of EUV observations from *STEREO-A*/EUVI from a limb-view perspective, we reconstruct the 3D geometry of the filament eruption and the underlying flare loops observed in EUV, SXR, and radio wavelengths. By assuming that the spike source makes a similar projection angle to the newly formed flare arcade where a radio gyrosynchrotron source is present, we reconstruct the 3D location of the spike source and place it well above the flare loops. In both *SDO*/AIA and *STEREO-A*/EUVI images, we identify supra-arcade fan-like structure in the close vicinity of the spike burst source, where multitudes of plasma downflows also occur. The speeds of the observed plasma downflows (∼227 km s^{-1} after de-projection) may be super-Alfvénic only if the magnetic field in the spike source region is sufficiently low ($\lesssim$15 G, if we take a plasma density of 2×10^{10} cm^{-3} for fundamental plasma radiation at 1.3 GHz). We also note that the downflows are only detected in AIA images ∼18 minutes after the spike bursts when the supra-arcade structures are more discernible, hence it is possible that the downflows have

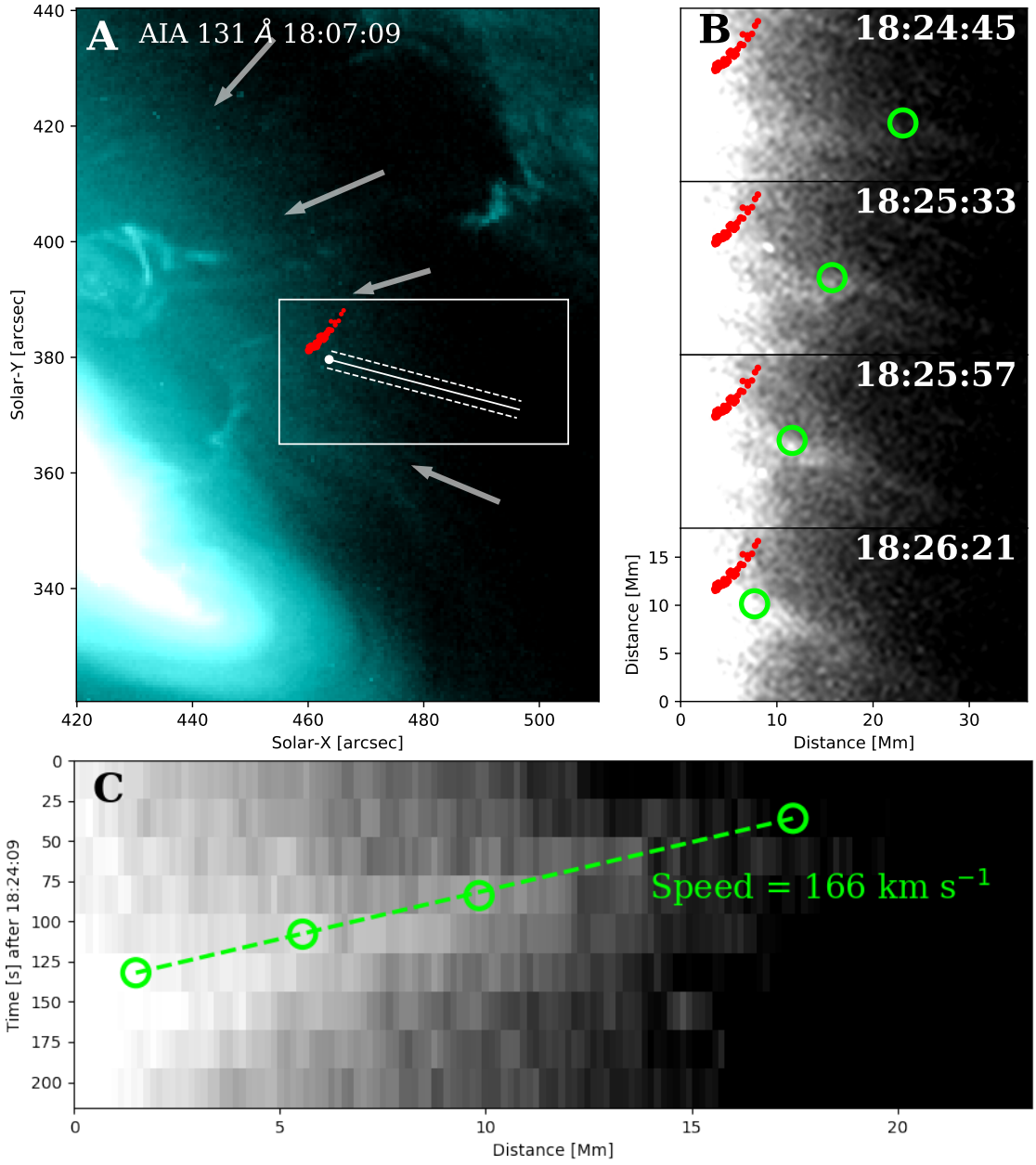

Figure 10. An example of plasma downflows observed in *SDO*/AIA 131 Å images. (A) Spike burst centroids at 18:07:07 UT (same as those in Fig. 3(E)) overlaid on AIA 131 Å. The diffuse SAF structure is indicated by white arrows. (B) An example plasma downflow observed in the vicinity of the spike burst at ∼18:25 UT. The field of view of the AIA 131 Å time-series images is indicated by a white box in (A). The images are overexposed to reveal the faint downflow feature. Green circles mark the leading front of the downflow. (C) Time-distance plot of the plasma downflow along the cut marked as a white line in (A; the distance starts from the location of the white dot and increases westward, or the right-hand side). The speed of the downflow in projection is about 166 km s^{-1}. An animation of the downflow from 18:23:57 UT to 18:29:33 UT is available online. The duration of the animation is 1 s.

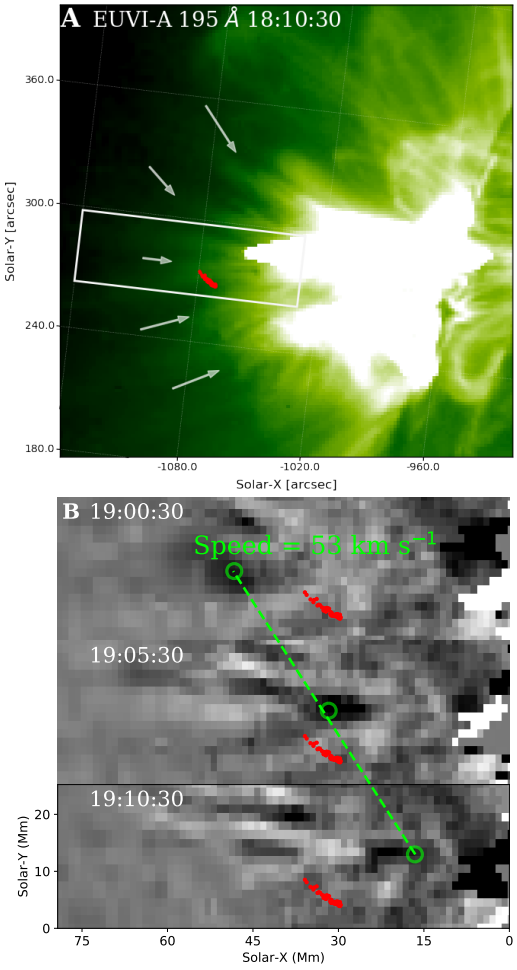

Figure 11. Example of plasma downflows observed in *SDO*/EUVI 195 Å images. (A) Spike burst location at 18:07:07 UT (same as those in Fig. 9(B)) overlaid on EUVI 195 Å. The diffuse SAF structure is indicated by white arrows. (B) An example plasma downflow observed in the vicinity of the spike burst at 19:00–19:10 UT. The field of view is indicated by a white box in (A). To show the downflow feature more clearly, running-ratio images are used. Note although the downflows are tracked using dark moving features (green circle) in the running-ratio images, similar to those in AIA 131 Å, they are in fact bright moving features in the original images. The speed in projection of this downflow is ∼53 km s^{-1}. An animation of the example downflow from 18:35:30 UT to 19:20:30 UT is available online. The duration of the animation is 2 s.

already slowed down substantially. If the plasma downflows at the time of the spike bursts are indeed sub-Alfvénic, it remains an outstanding question whether the observed plasma flows are indeed signatures of the reconnection outflows themselves that drive the termination shock or, instead, are structures in the outflows which are substantially slower due to, e.g., an aerodynamic drag force (Savage & McKenzie 2011; Longcope et al. 2018; Yu et al. 2020).

Based on the observational evidence discussed above, we conclude that our observations are generally consistent with the scenario proposed by Chen15: A flare termination shock is formed at the front of reconnection outflows above the flare arcade. The observed spike bursts are due to coherent radio emission from nonthermal electrons in either the upstream or downstream region of the shock front. The schematic illustration in Fig. 12 summarizes our observations of a variety of features in the flare reconnection picture during the extended energy release phase. However, unlike the limb event in Chen15, this event is viewed against the disk. Although we have demonstrated that the spike source is located well-above the flare loops in a supra-arcade fan region, the exact relationship between the spike source and the flare geometry is unclear. This is largely due to the unfavorable viewing geometry for seeing the newly reconnected, presumably cusp-shaped field lines between the shock front and the flare loops (cyan curves in Figure 12). On the other hand, the cooling flare loops seen two hours later below the spike burst location is a possible indication for the presence of these newly reconnected field lines.

Another intriguing difference is the spatial separation between the spike source and the looptop SXR/radio sources in this event (∼70″ in projection and similar in radial height if we adopt a projection angle of 43°) is much larger than the ∼8″ separation between the spike source and the HXR looptop source reported in Chen15. Theoretical studies of the flare termination shock suggest that the shock occurs above the flare arcades where there is a sharp gradient in flow speed—i.e., where the supermagnetosonic reconnection outflows are "terminated" as they impinge upon the dense, previously reconnected plasma above the looptops. The exact location of the shock front, however, depends on a variety of factors including the flare geometry, properties of the reconnection diffusion region, and flow speeds in the shock upstream and downstream (Forbes 1986). As shown by recent numerical results in Cai et al. (2019), early in the flare, the shock occurs at a relatively low position above the looptops. At later times into the flare, after more and more reconnected magnetic flux (and plasma) piled up in the looptop region, the distance between the shock front and the looptop appears to grow significantly (c.f., their Figure 14(f)). For our event, as the spike bursts are observed well into the extended energy release phase (∼25 min after the SXR peak), it is possible that the termination shock front is located at a substantial distance away from the top of the flare ar-

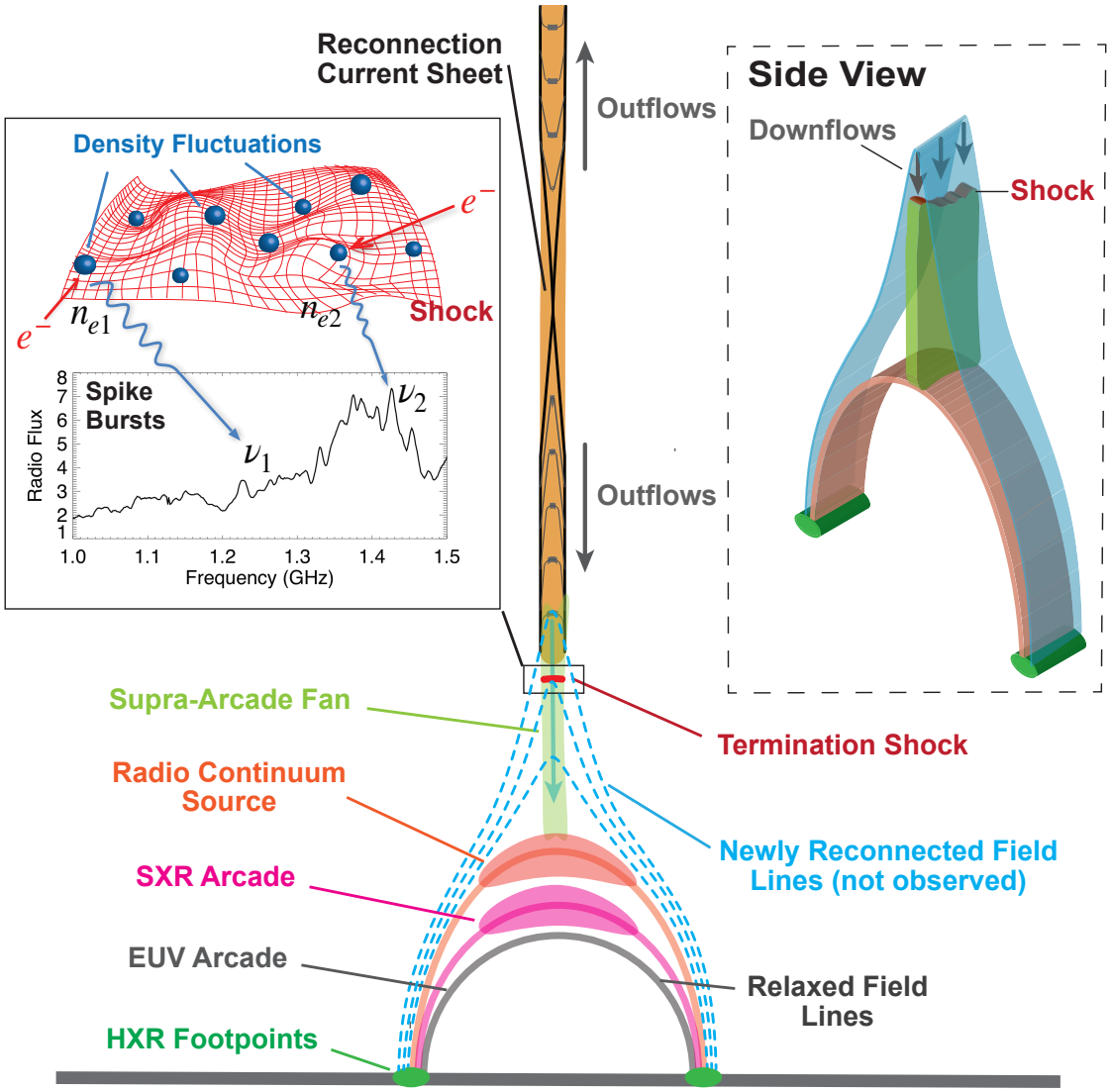

Figure 12. Schematic illustration of observed phenomena during the extended energy release phase of the eruptive flare event. A filament eruption induces magnetic reconnection in a large-scale current sheet. Downward-propagating reconnection outflows impinge upon the newly reconnected flare loops, forming a termination shock within the supra-arcade fan region where highly bent, newly reconnected magnetic field lines are formed. The shock and the supra-arcade fan are located above the radio continuum source (orange curve), SXR arcade (magenta curve), and EUV arcade (grey curve). The observed radio spike bursts are produced at the shock front where nonthermal electrons interact with density flutuations (inset on the left; after Chen15 and Chen19). Accelerated electrons propagating downward along the flare arcade produce the conjugate HXR footpoints and (E)UV flare ribbons. Inset on the right shows a side view of the lower portion of the schematic.

cades, similar to those reported in earlier works when the radio signature was detected late in the flare (e.g., Aurass & Mann 2004).

Finally, we note that there are several unanswered questions in the interpretation of the observations in terms of the flare termination shock scenario. One question is on why the stochastic spike bursts do not usually coincide with the peak of the flare energy release and, in fact, are only occasionally reported within a limited period (see also Aurass et al. 2002; Aurass & Mann 2004). We attribute the rather uncommon appearance of these spikes to a) the requirements for generating a fast-mode flare termination shock, which may only be met in certain locations and times (not necessarily the impulsive energy release phase) in the looptop region where the outflow speed exceeds the local fast-mode magnetosonic speed (e.g., Shen et al. 2018). and b) the special conditions for producing the coherent radio emission. Chen15 suggests a linear mode conversion mechanism due to Langmuir waves interacting with small-scale density fluctuations. The mechanism requires 1) the excitation and nonlinear growth of Langmuir waves,

and 2) the subsequent interactions with the turbulent medium. Both conditions are not universally fulfilled throughout the shock region. The second intriguing question is on the requirement of a localized dense region in the spike source that has a plasma density of order 10^{10} cm^{-3} (suggested by the plasma radiation mechanism). Although we argue that such a plasma density in the above-the-looptop region is not inconsistent with the flare context (Appendix A), it may require some addition localized density enhancement or compression. The lack of a strong EUV emission in this region suggests that each of the density fluctuations on the shock surface may be too compact to have a sufficient large differential emission measure so as to be distinguished against the coronal background (see, e.g., Chen et al. 2013 for similar discussions on the absence of type-III-radio-burst-emitting coronal loops in EUV images). Another question is on the apparent frequency gradient along the shock surface (c.f., Figure 3(E)), which presumably corresponds to a localized density gradient. Such a density gradient may be attributed to the spatiotemporal variations of the shock properties along the shock front (Chen et al. 2019). Last but not least, as discussed earlier, the seemly sub-Alfvénic plasma downflows (albeit observed at much later times) and the absence of strong modulations of the spike-centroid-illuminated shock front as those reported in Chen15 both call for further investigation. For the latter, based on MHD simulations, Shen et al. (2018) suggested that the shock dynamics is intimately related to the details of the plasma-outflow–shock-front interactions.

In order to answer the questions above and gain a more comprehensive understanding on the formation of the flare termination shocks and their associated radio emission, more observations made with radio dynamic spectroscopic imaging are required. Complementary high-resolution, high-cadence EUV/X-ray imaging and spectroscopic observations, as well as 3D numerical simulations, are also particularly helpful for understanding the essential physical context in the vicinity of the shock, including SAF structures, plasma outflows, and the hot flare arcades.

APPENDIX

A. X-RAY SPECTRAL ANALYSIS

We perform RHESSI X-ray spectral analysis based on data from 18:00:35 UT to 18:03:33 UT (time interval 2) using front segments of detectors 1, 3, 5, 6, 7, 8 and 9 separately. The attenuator state within the selected time interval is A1. A pileup check is performed with `hsi_pileup_check.pro` in `SSWIDL`, which suggests a small, but non-negligible pileup effect. The background time is selected as 20:30:00 UT to 20:31:00 UT (during RHESSI night; purple curve in Figure 13). By examining the spectra from various detectors, we suspect that there could be additional background contribution to the counts above ∼40 keV that is unaccounted for by the nominal background derived from the selected interval. Therefore, we restrict the fit range to 6–40 keV.

For the spectral fit, we adopt an isothermal model for the thermal plasma, a thick-target model with a single power-law distribution for the nonthermal electrons, as well as a pileup component. The fit results and parameters from 7 different detectors are generally consistent with each other. An example from detector 7 is shown in Figure 13. For the thermal component contributed by the SXR flare arcade (green curve), the average plasma temperature across the 7 detectors is 19 MK (the full range is 18–20 MK) and the average volume emission measure is $\mathrm{EM_V} \approx 7.8 \times 10^{48}$ cm^{-3} (the full range is $6.9-9.1\times10^{48}$ cm^{-3}). We take the 50% contour of the 12–15 keV SXR flare arcade source to estimate a source area of $A \approx 38'' \times 19'' \approx 3.8\times10^{18}$ cm^{-3}. If we take the column depth of the SXR arcade to be the same as its width, we estimate a volume of $V \approx 5.3\times10^{27}$ cm^3. The thermal density is hence $n_{\rm th} = (\mathrm{EM}_V/V)^{1/2} \approx 3.8\times10^{10}$ cm^{-3}, which is about two times the inferred plasma density of the spike burst source for fundamental plasma radiation at 1.3 GHz (2×10^{10} cm^{-3}). We conclude that the density of the spike source is not inconsistent with the flare context, particularly if a large density scale height (e.g., a typical flare temperature of 10 MK corresponds to a hydrostatic scale height of ∼500 Mm) and/or a localized density enhancement or compression is present at the spike burst site.

This work makes use of public VLA data from the observing program VLA/11B-129. The authors acknowledge Richard Perley, Michael Rupen, Ken Sowinski, Stephen White for their help in carrying out the observing program. The NRAO is a facility of the National Science Foundation (NSF) operated under cooperative agreement by Associated Universities, Inc. This work is supported partly by NASA grant NNX17AB82G and NSF grants AGS-1654382, AGS-1723436, and AST-1735405 to New Jersey Institute of Technology. We thank Lucia Kleint and Marina Battaglia for providing us the original version of the 3D ellipse loop fitting codes. We also thank Chengcai Shen and Kathy Reeves for helpful discussions.

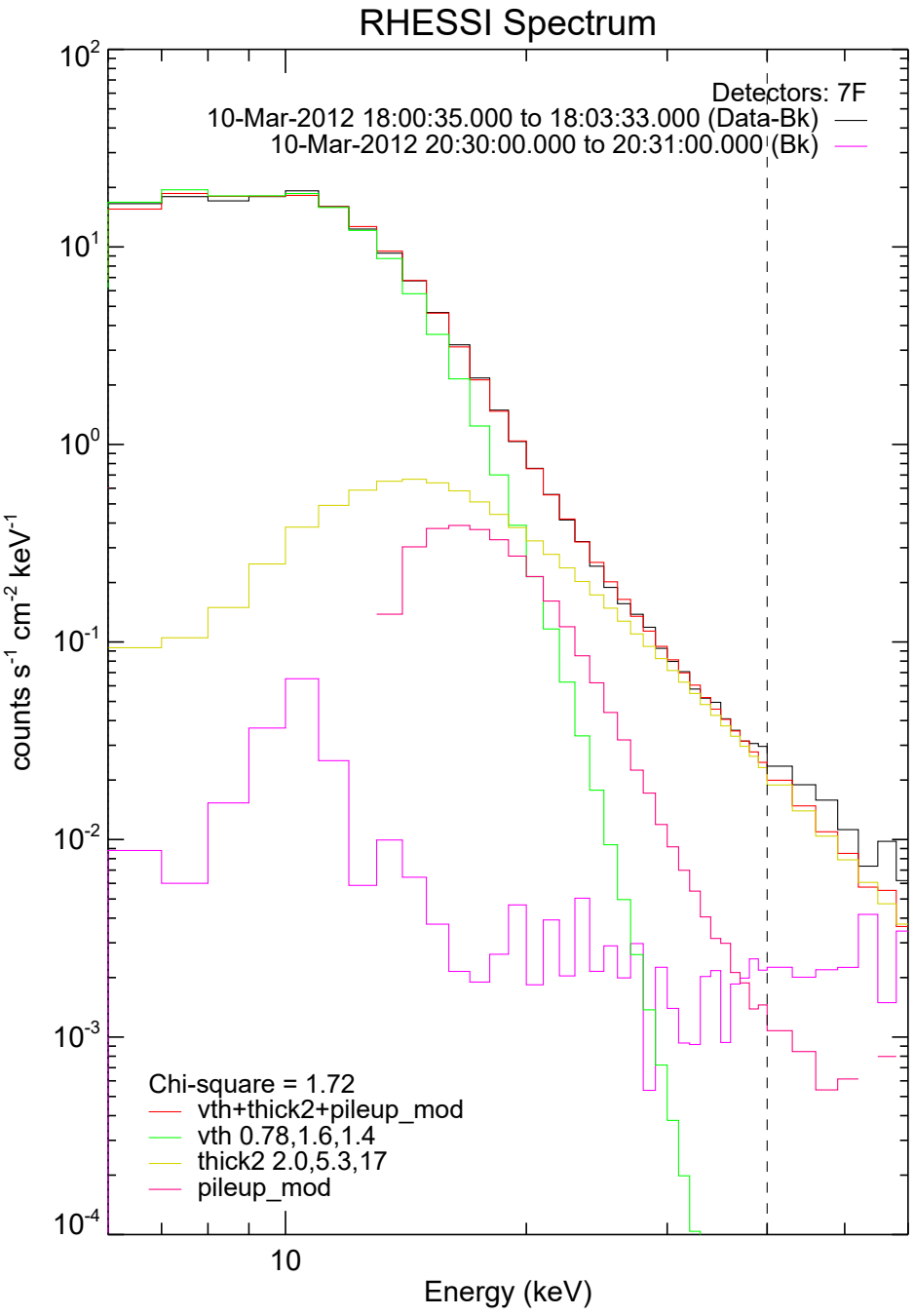

Figure 13. RHESSI X-ray spectral analysis of detector 7 for time interval 2 (18:00:35 UT–18:03:33 UT, as marked in Figure 2(A)). For the thermal component ("vth"; green curve), three fit parameters (indicated in the legend) are volume emission measure ($EM_V = 7.8 \times 10^{48}$ cm^{-3}), plasma temperature (1.6 keV, or 19 MK), and relative abundance (1.4). For the thick-target model, we adopt a single power-law distribution for the nonthermal electrons. Three fit parameters are total integrated electron flux (2.0×10^{35} sec^{-1}), power-law index of the electron flux spectrum ($\delta = 5.3$), and low-energy cutoff (17 keV). The high energy cutoff is fixed to 1 MeV. A pileup component is also included in the spectral fit. The upper limit of the fit is restricted to 40 keV to avoid the possible contribution of the background at higher energies. See Appendix for details.

Facilities: VLA, SDO, STEREO, RHESSI

Software: CASA (McMullin et al. 2007), Astropy (Astropy Collaboration et al. 2018), SunPy (The SunPy Community et al. 2020)

REFERENCES

Ajello, M., Albert, A., Allafort, A., et al. 2014, ApJ, 789, 20

Altyntsev, A. T., Grechnev, V. V., Zubkova, G. N., et al. 1995, A&A, 303, 249

Aschwanden, M. J. 2002, SSRv, 101, 1

Astropy Collaboration, Price-Whelan, A. M., Sipőcz, B. M., et al. 2018, AJ, 156, 123

Aulanier, G., Démoulin, P., Schrijver, C. J., et al. 2013, A&A, 549, A66

Aulanier, G., Janvier, M., & Schmieder, B. 2012, A&A, 543, A110

Aurass, H., & Mann, G. 2004, ApJ, 615, 526

Aurass, H., Vršnak, B., & Mann, G. 2002, A&A, 384, 273

Battaglia, M., & Benz, A. O. 2009, A&A, 499, L33

Benz, A. O. 1986, SoPh, 104, 99

Benz, A. O., Grigis, P. C., Csillaghy, A., & Saint-Hilaire, P. 2005, SoPh, 226, 121

Benz, A. O., Jaeggi, M., & Zlobec, P. 1982, A&A, 109, 305

Benz, A. O., Saint-Hilaire, P., & Vilmer, N. 2002, A&A, 383, 678

Blandford, R. D., & Ostriker, J. P. 1978, ApJL, 221, L29

Burgess, D., Möbius, E., & Scholer, M. 2012, SSRv, 173, 5

Cai, Q., Shen, C., Raymond, J. C., et al. 2019, MNRAS, 489, 3183

Cargill, P. J., Mariska, J. T., & Antiochos, S. K. 1995, ApJ, 439, 1034

Carley, E. P., Hayes, L. A., Murray, S. A., et al. 2019, Nature Communications, 10, 2276

Chen, B., Bastian, T. S., & Gary, D. E. 2014, ApJ, 794, 149

Chen, B., Bastian, T. S., Shen, C., et al. 2015, Science, 350, 1238

Chen, B., Bastian, T. S., White, S. M., et al. 2013, ApJL, 763, L21

Chen, B., Shen, C., Reeves, K. K., Guo, F., & Yu, S. 2019, ApJ, 884, 63

Chen, B., Yu, S., Reeves, K. K., & Gary, D. E. 2020a, ApJL, 895, L50

Chen, B., Yu, S., Battaglia, M., et al. 2018, ApJ, 866, 62

Chen, B., Shen, C., Gary, D. E., et al. 2020b, Nature Astronomy, 4, 1140

Cheng, J. X., & Qiu, J. 2016, ApJ, 825, 37

Cheng, X., Ding, M. D., Zhang, J., et al. 2014, ApJL, 789, L35

Chintzoglou, G., Patsourakos, S., & Vourlidas, A. 2015, ApJ, 809, 34

Chrysaphi, N., Kontar, E. P., Holman, G. D., & Temmer, M. 2018, ApJ, 868, 79

Cliver, E. W., White, S. M., & Balasubramaniam, K. S. 2011, ApJ, 743, 145

Condon, J. J. 1997, PASP, 109, 166

Csillaghy, A., & Benz, A. O. 1993, A&A, 274, 487

Dhakal, S. K., Chintzoglou, G., & Zhang, J. 2018, ApJ, 860, 35

Dhakal, S. K., Zhang, J., Vemareddy, P., & Karna, N. 2020, arXiv e-prints, arXiv:2008.03447

Dulk, G. A., & Marsh, K. A. 1982, ApJ, 259, 350

Elmhamdi, A., Romano, P., Kordi, A. S., & Al-trabulsy, H. A. 2014, SoPh, 289, 2957

Fleishman, G. D., Gary, D. E., & Nita, G. M. 2003, ApJ, 593, 571

Fleishman, G. D., & Kuznetsov, A. A. 2010, ApJ, 721, 1127

Fletcher, L. 2009, A&A, 493, 241

Fomichev, V., & Chernov, G. 2020, ApJ, 901, 65

Forbes, T. G. 1986, ApJ, 305, 553

—. 1988, SoPh, 117, 97

Forbes, T. G., & Acton, L. W. 1996, ApJ, 459, 330

Forbes, T. G., & Malherbe, J. M. 1986, ApJL, 302, L67

Gallagher, P. T., Dennis, B. R., Krucker, S., Schwartz, R. A., & Tolbert, A. K. 2002, SoPh, 210, 341

Gary, D. E., Hurford, G. J., & Flees, D. J. 1991, ApJ, 369, 255

Gary, D. E., Chen, B., Dennis, B. R., et al. 2018, ApJ, 863, 83

Guedel, M., Benz, A. O., & Aschwanden, M. J. 1991, A&A, 251, 285

Guo, F., & Giacalone, J. 2012, ApJ, 753, 28

Guo, L., Li, G., Reeves, K., & Raymond, J. 2017, ApJL, 846, L12

Hanneman, W. J., & Reeves, K. K. 2014, ApJ, 786, 95

Howard, R. A., Moses, J. D., Vourlidas, A., et al. 2008, SSRv, 136, 67

Innes, D. E., Guo, L. J., Bhattacharjee, A., Huang, Y. M., & Schmit, D. 2014, ApJ, 796, 27

Janvier, M., Aulanier, G., Bommier, V., et al. 2014, ApJ, 788, 60

Janvier, M., Aulanier, G., & Démoulin, P. 2015, SoPh, 290, 3425

Janvier, M., Aulanier, G., Pariat, E., & Démoulin, P. 2013, A&A, 555, A77

Ji, H., Wang, H., Schmahl, E. J., Moon, Y. J., & Jiang, Y. 2003, ApJL, 595, L135
Kaiser, M. L., Kucera, T. A., Davila, J. M., et al. 2008, SSRv, 136, 5
Karlický, M., Sobotka, M., & Jiřička, K. 1996, SoPh, 168, 375
Kong, X., Guo, F., Shen, C., et al. 2020, ApJL, 905, L16
—. 2019, ApJL, 887, L37
Kontar, E. P., Yu, S., Kuznetsov, A. A., et al. 2018, Nature Communications, 9, 146
Kouloumvakos, A., Patsourakos, S., Nindos, A., et al. 2016, ApJ, 821, 31
Krucker, S., Aschwanden, M. J., Bastian, T. S., & Benz, A. O. 1995, A&A, 302, 551
Krucker, S., Battaglia, M., Cargill, P. J., et al. 2008, A&A Rv, 16, 155
Leibacher, J., Sakurai, T., Schrijver, C. J., & van Driel-Gesztelyi, L. 2010, SoPh, 263, 1
Lemen, J. R., Title, A. M., Akin, D. J., et al. 2012, SoPh, 275, 17
Li, G., Kong, X., Zank, G., & Chen, Y. 2013, ApJ, 769, 22
Lin, J., & Forbes, T. G. 2000, J. Geophys. Res., 105, 2375
Liu, Y. D., Richardson, J. D., Wang, C., & Luhmann, J. G. 2014, ApJL, 788, L28
Longcope, D., Unverferth, J., Klein, C., McCarthy, M., & Priest, E. 2018, ApJ, 868, 148
Magara, T., Mineshige, S., Yokoyama, T., & Shibata, K. 1996, ApJ, 466, 1054
Magdalenić, J., Marqué, C., Krupar, V., et al. 2014, ApJ, 791, 115
Mann, G., Warmuth, A., & Aurass, H. 2009, A&A, 494, 669
Masuda, S., Kosugi, T., Hara, H., Tsuneta, S., & Ogawara, Y. 1994, Nature, 371, 495
McMullin, J. P., Waters, B., Schiebel, D., Young, W., & Golap, K. 2007, in Astronomical Society of the Pacific Conference Series, Vol. 376, Astronomical Data Analysis Software and Systems XVI, ed. R. A. Shaw, F. Hill, & D. J. Bell, 127
Miklenic, C., Veronig, A. M., Temmer, M., Möstl, C., & Biernat, H. K. 2011, SoPh, 273, 125
Miller, J. A., Cargill, P. J., Emslie, A. G., et al. 1997, J. Geophys. Res., 102, 14631
Mohan, A., & Oberoi, D. 2017, SoPh, 292, 168
Nishizuka, N., & Shibata, K. 2013, PhRvL, 110, 051101
O'Dwyer, B., Del Zanna, G., Mason, H. E., Weber, M. A., & Tripathi, D. 2010, A&A, 521, A21
Paesold, G., Benz, A. O., Klein, K. L., & Vilmer, N. 2001, A&A, 371, 333
Park, J., Ren, C., Workman, J. C., & Blackman, E. G. 2013, ApJ, 765, 147
Patsourakos, S., Georgoulis, M. K., Vourlidas, A., et al. 2016, ApJ, 817, 14
Perley, R. A., Chandler, C. J., Butler, B. J., & Wrobel, J. M. 2011, ApJL, 739, L1
Pesnell, W. D., Thompson, B. J., & Chamberlin, P. C. 2012, SoPh, 275, 3
Polito, V., Galan, G., Reeves, K. K., & Musset, S. 2018, ApJ, 865, 161
Qiu, J., Liu, W., Hill, N., & Kazachenko, M. 2010, ApJ, 725, 319
Reeves, K. K., Freed, M. S., McKenzie, D. E., & Savage, S. L. 2017, ApJ, 836, 55
Reeves, K. K., Polito, V., Chen, B., et al. 2020, arXiv e-prints, arXiv:2010.12049
Reeves, K. K., Seaton, D. B., & Forbes, T. G. 2008, ApJ, 675, 868
Reid, M. J., Schneps, M. H., Moran, J. M., et al. 1988, ApJ, 330, 809
Reynolds, S. P. 2008, ARA&A, 46, 89
Savage, S. L., & McKenzie, D. E. 2011, ApJ, 730, 98
Seaton, D. B., & Forbes, T. G. 2009, ApJ, 701, 348
Sharma, R., Battaglia, M., Luo, Y., Chen, B., & Yu, S. 2020, ApJ, 904, 94
Shen, C., Kong, X., Guo, F., Raymond, J. C., & Chen, B. 2018, ApJ, 869, 116
Shibata, K., Masuda, S., Shimojo, M., et al. 1995, ApJL, 451, L83
Slottje, C. 1978, Nature, 275, 520
Somov, B. V., & Kosugi, T. 1997, ApJ, 485, 859
Sterling, A. C., & Hudson, H. S. 1997, ApJL, 491, L55
Takahashi, T., Qiu, J., & Shibata, K. 2017, ApJ, 848, 102
Takasao, S., Matsumoto, T., Nakamura, N., & Shibata, K. 2015, ApJ, 805, 135
Takasao, S., & Shibata, K. 2016, ApJ, 823, 150
Tan, B., Chen, N., Yang, Y.-H., et al. 2019, ApJ, 885, 90
The SunPy Community, Barnes, W. T., Bobra, M. G., et al. 2020, The Astrophysical Journal, 890, 68. https://iopscience.iop.org/article/10.3847/1538-4357/ab4f7a
Török, T., & Kliem, B. 2005, ApJL, 630, L97
Tsuneta, S. 1996, ApJ, 456, 840
Tsuneta, S., Hara, H., Shimizu, T., et al. 1992, PASJ, 44, L63
Tsuneta, S., & Naito, T. 1998, ApJL, 495, L67
Wang, R., Liu, Y. D., Yang, Z., & Hu, H. 2014, ApJ, 791, 84
Wang, Z., Chen, B., & Gary, D. E. 2017, ApJ, 848, 77
Warmuth, A., Mann, G., & Aurass, H. 2009, A&A, 494, 677
Workman, J. C., Blackman, E. G., & Ren, C. 2011, Physics of Plasmas, 18, 092902

Wuelser, J.-P., Lemen, J. R., Tarbell, T. D., et al. 2004, in Society of Photo-Optical Instrumentation Engineers (SPIE) Conference Series, Vol. 5171, Proc. SPIE, ed. S. Fineschi & M. A. Gummin, 111–122

Yu, S., & Chen, B. 2019, ApJ, 872, 71

Yu, S., Chen, B., Reeves, K. K., et al. 2020, ApJ, 900, 17

Zarro, D. M., Sterling, A. C., Thompson, B. J., Hudson, H. S., & Nitta, N. 1999, ApJL, 520, L139

Zharkova, V. V., Arzner, K., Benz, A. O., et al. 2011, SSRv, 159, 357

Zheng, J.-C., Yang, Z.-L., Guo, J.-P., et al. 2017, Research in Astronomy and Astrophysics, 17, 081

Zimovets, I., Vilmer, N., Chian, A. C. L., Sharykin, I., & Struminsky, A. 2012, A&A, 547, A6

Zucca, P., Morosan, D. E., Rouillard, A. P., et al. 2018, A&A, 615, A89